KINETICS AND APPLICATIONS OF ON-SURFACE TOPOCHEMICAL POLYMERIZATION OF DIACETYLENE STRIPED PHASES

by

Anni Shi

A Dissertation

Submitted to the Faculty of Purdue University

In Partial Fulfillment of the Requirements for the degree of

Doctor of Philosophy

Department of Chemistry

West Lafayette, Indiana

May 2022

THE PURDUE UNIVERSITY GRADUATE SCHOOL
STATEMENT OF COMMITTEE APPROVAL

Dr. Shelley A. Claridge, Chair

Department of Chemistry

Department of Biomedical Engineering

Dr. Christina W. Li

Department of Chemistry

Dr. Suzanne Bart

Department of Chemistry

Dr. Chi Zhang

Department of Chemistry

Approved by:

Dr. Christine Hrycyna

Dedicated to my parents, whose genetic and environmental impacts make this happens

ACKNOWLEDGMENTS

Condensed with learning and personal growth, here my PhD journey ends. It is my privilege to be surrounded with sincere mentorship and supports from amazing people. With apologies to anyone I fail to mention, I acknowledge a few of those people here.

I dedicate my most gratitude to my advisor Professor Shelley Claridge. She shows me the great merits of an excellent scientist and team leader. Beyond patient and inspiring academic guidance, I am impressed and influenced by her passionate drive for perfection in science, and tactful management with our research group. Her practical optimism encourages me to continue my scientific research and to take responsibilities to uplift research society with other scientists. I will forever appreciate her mentorship for the past 5 years.

I am grateful to meet my friendly and like-minded labmates in Claridge lab. I especially thank Dr. Jae Jin Bang and Dr. Tyler Hayes; their selfless support and guidance helped me to establish a good mindset of a responsible scientist and a valuable team player in the early years of my PhD. I am grateful to Dr. Shane Russell, Dr. Terry Villarreal, Dr. Tyson Davis and Dr. Jeremiah Bechtold; my knowledge and logics of research has improved during the countless but delightful discussions with them. I should never forget to mention the invaluable companion offered by Erin Lang, Laura Williams, and Anamika Singh; I am fortunate to learn among my intelligent and collaborative peers. It was my great pleasure to mentor Juan Arango, Chris Pintro and Joseph Garfield; I appreciate their trust from the bottom of my heart.

I am grateful for the kindness of my friends. My appreciation outwins words about the enlightening advice and encouraging companion from Dr. Judy Liu, and the intelligently sarcastic conversations with Elizabeth Chu. I appreciate the friendly and supportive environment of graduate students from Greater China community in my department; their friendship shields me from the anxiety from disconnection. I would also like to thank for my bold friends Billy He and Yiying Zhao, whom I encountered in the early and late stage of my PhD years, respectively; their sparkling inspirations help me to overcome my circumspect personality.

Lastly, my utmost appreciation and respect are bestowed to my parents. They endowed my life and present me with merits of being human in the complex world. The persistence and resistance, empathy and compassion, which I inherit and learn from them, will carry me beyond this point, will succor me to survive in the unpredictable future.

TABLE OF CONTENTS

LIST OF FIGURES 7
ABSTRACT 10
CHAPTER 1. INTRODUCTION 12
CHAPTER 2. DESIGN PRINCIPLES FOR ACCELERATING AN ON-SURFACE POLYMERIZATION, CHARACTERIZED FROM SINGLE-POLYMER TO MICROSCOPIC SCALES 16
2.1 Introduction 16
2.2 Results and Discussion 19
2.2.1 Preparation of striped phase monolayer 19
2.2.2 Measurements of striped phase PDA polymerization 20
2.2.3 Impact of alkyl terminal segments on polymerization efficiency 23
2.2.4 Contact angle titrations of diynoic acid monolayers on HOPG 27
2.3 Conclusion 29
2.4 Experimental Methods 29
2.4.1 Materials 29
2.4.2 Formation of striped phase monolayers via Langmuir-Schaefer transfer. 30
2.4.3 Atomic force microscope (AFM) imaging and image processing 30
2.4.4 Analysis of AFM images for assessment of polymerization on HOPG. 31
2.4.5 Scanning electron microscope (SEM) imaging 32
2.4.6 Confocal fluorescence microscopy and spectral imaging 32
2.4.7 Analysis of fluorescence at different timepoints 33
2.4.8 Molecular modeling 37
CHAPTER 3. POLYMERIZATION OF ALKYLDIYNAMINE STRIPED PHASES ON 2D MATERIALS: A ROUTE TO 1-NM-RESOLUTION REACTIVE FUNCTIONAL PATTERNS AT INTERFACES 42
3.1 Introduction 42
3.2 Results and Discussion 44
3.2.1 Preparation of striped phase monolayers 44
3.2.2 Comparison of polymerization of TCD-NH_2 and PCD-NH_2. 46

3.2.3 Impact of terminal segments on chain propagation. 49
3.2.4 Calculations of probability of sPDA transfer to PDMS based on PDA length 50
3.2.5 Applications of -NH_2 functional arrays on PDMS surfaces 52
3.3 Conclusion 54
3.4 Experimental Methods 55
3.4.1 Materials 55
3.4.2 Langmuir-Schaefer transfer to generate striped alkyldiynamine films 56
3.4.3 Preparation of PDMS stamps 57
3.4.4 Microcontact printing (μCP) of alkydiynamines 57
3.4.5 Covalent transfer of striped phase polydiacetylene layers from HOPG to PDMS 57
3.4.6 Synthesis of CdSe nanoparticles (NPs) 58
3.4.7 Specific adsorption of CdSe NPs on PCD-NH_2 58
3.4.8 Functionalization of PCD-NH2 with Rhodamine Red-X (RR) succinimidyl ester 59
3.4.9 Atomic force microscopy (AFM) imaging and image analysis 59
3.4.10 Scanning electron microscopy (SEM) imaging 59
3.4.11 Confocal fluorescence microscopy and spectral imaging 60
3.4.12 Wide-field fluorescence microscopy 60
3.4.13 Molecular modeling 61
3.4.14 Image analysis 61
3.4.15 Measurement of degree of polymerization 61
3.4.16 Calculation of PDMS transfer probabilities of polymers 62
3.4.17 Analysis of fluorescence images. 66
REFERENCES 70

LIST OF FIGURES

Figure 2.1 Schematics of (a) polymerization of a diacetylene striped phase on HOPG, and (b) of transfer to PDMS. Cartoon representation of (c) characterization of polymerization by AFM on HOPG, and by fluorescence on PDMS, and (d) of comparison between monomers..... 18

Figure 2.2 (a, b) Molecular models of unpolymerized and polymerized PCDA monolayers on HOPG (PCDA/HOPG); (c) AFM image of unpolymerized PCDA/HOPG; (d) AFM image of polymerized PCDA/HOPG showing "lifted" PDA; (e) SEM image of domain structure of polymerized PCDA/HOPG. 20

Figure 2.3 (a,b) Schematics of PDA transfer to PDMS; (c,d) Fluorescence (c) images and (d) emission spectra of striped TCDA and PCDA monolayers on PDMS; (e, f) Measurement of polymerization conversion by AFM (main image) and fluorescence microscopy (inset). Note that different timepoints are shown for TCDA (0, 20, 60 min) and PCDA (0, 60, 90 min) images, in order to illustrate similar conversion. AFM images are processed to the same color scale (full range = 1.8 nm), with the lower height areas of the monolayers set to equivalent height in each image. Scale bars in fluorescence insets are all 20 μm..... 22

Figure 2.4 (a-d) AFM images of (a,b) TCDA/HOPG and (c,d) PCDA/HOPG at low (a, c) and high (b, d) conversion. (e) Histograms of number average and weight average degrees of polymerization at low and high conversion..... 24

Figure 2.5 Molecular models of PCDA and TCDA polymerization. (a) Illustration of oligomer compression to simulate lattice mismatch. (b,c) Illustration and graph of differences in distances between bond-forming carbons at oligomer top and bottom. (d-f) Illustration of difference in alkyl chain packing distance near chain ends..... 26

Figure 2.6 (a) Contact angle titration curves for polymerized 10,12-PCDA (blue), 10,12-TCDA (red), 10,12-HCDA (orange), and 10,12-NDDA (green). Difference between pre- and post-polymerization contact angles in advancing (top right) and receding (bottom right) measurements. (b) Structure of 8,10-HCDA and contact angle titration curves for polymerized 8,10-HCDA (gold), 10,12-PCDA (blue), 8,10-TCDA (red), and 10,12-NDDA (green). (c,d) AFM and (e,f) fluorescence images of (c,e) 8,10-HCDA and (d,f) 10,12-HCDA, illustrating more extensive polymerization of 8,10-HCDA at both timepoints. (f) Contact angle titration curves for polymerized 10,12-PCDA (blue), 8,10-TCDA (red), 8,10-HCDA (orange), and 10,12-NDDA (green). Difference between pre- and post-polymerization contact angles in advancing (top right) and receding (bottom right) measurements. 28

Figure 2.7 .Mean and standard deviation fluorescence values for regions of interest collected on PCDA/PDMS samples at the indicated polymerization timepoints. 15-30 regions were collected at each timepoint from 3–6 samples. Outliers identified through the quartile analysis are italicized. 34

Figure 2.8 Statistical analysis of fluorescence emission from TCDA/PDMS regions of interest analyzed at each timepoint. In the manuscript, data are graphed with error bars representing the 25th percentile (Q1) and 75th percentile (Q3) of data values. 35

Figure 2.9 Mean and standard deviation fluorescence values for regions of interest collected on TCDA/PDMS samples at the indicated polymerization timepoints. 15-30 regions were collected at each timepoint from 3–6 samples. Outliers identified through the quartile analysis are italicized. 36

Figure 2.10 Statistical analysis of fluorescence emission from PCDA/PDMS regions of interest analyzed at each timepoint. In the manuscript, data are graphed with error bars representing the 25th percentile (Q1) and 75th percentile (Q3) of data values. 37

Figure 2.11 Energetically minimized PCDA models of initial state and displacement steps 2, 4 and 8. 40

Figure 2.12 Energetically minimized TCDA models of initial state and displacement steps 2, 4, 8 and 11. 41

Figure 3.1 (a) Illustration of striped phase assembly on HOPG and (b) subsequent transfer of sPDAs to PDMS for nm-resolution functional patterning. (c) Illustration of use of fluorescence to characterize polymerization efficiency of NH_2 striped phases in comparison with COOH striped phases. (d) Illustration of probabilistic model for predicting sPDA transfer efficiency. 44

Figure 3.2 (a, b) Molecular models of (a) unpolymerized and (b) pol-ymerized PCD-NH_2 striped phases on HOPG, highlighting lamellar width. (c, d) AFM images of (c) unpolymerized and (d) polymerized PCD-NH_2. Arrows in (c) illustrate lameller axes in two domains oriented epitaxially with the HOPG lattice. Inset in (c) is a line scan acquired at the white line segment in (c). Inset in (d) illustrates topographic protrusion corresponding to 'lifted' sPDA backbone. (e) SEM image of PCD-NH_2 domains, showing lamellar axis revealed by cracks in monolayer. 46

Figure 3.3 (a) Schematic of sPDA transfer to PDMS. (b) Fluorescence emission spectrum of PCD-NH_2/PDMS showing excitonic peak and vibrational sidebands. (c) Measurement of fluorescence emission for TCD-NH_2 and PCD-NH_2 transferred to PDMS following photopolymerization on HOPG for stated time; curve fits of previously measured values for structurally comparable carboxylic acids (TCD-COOH and PCD-COOH) are shown in dashed and dotted grey lines, respectively. Representative fluorescence images at selected timepoints (0, 35, 60 min) are also shown. (d) Molecular models of conformational change associated with polymerization of PCD-NH_2 (top) and PCD-COOH (bottom). 48

Figure 3.4 . (a, b) AFM images of polymerized (a) TCD-NH_2 and (b) PCD-NH_2 at low conversion timepoints; (c, d) Distribution of polymer lengths of PCD-NH_2 and TCD-NH_2. 50

Figure 3.5 (a) Schematic illustrating structural factors predicted to impact transfer efficiency of sPDA transfer to PDMS. (b) Predicted transfer efficiencies for TCD-NH_2 and PCD-NH_2, within a selected range of per-subunit reaction probabilities (p_{rxn}) and number of crosslinks required for transfer (n). (c) Predicted ratio of TCD-NH_2 to PCD-NH_2 transfer. (d) Predicted fractional transfer vs number of sPDA repeat units, if at least 2 crosslink is required for transfer (left,gold), or if at least 3 (center, red) or 4 (right, green) crosslinks are required. 51

Figure 3.6 (a) Schematic of nanocrystal binding to striped PCD-NH_2/PDMS. (b) TEM image of CdSe nanocrystals used in adsorption experiment. (c) AFM phase images of (bottom) (top) CdSe/PCD-NH_2 and PCD-NH_2 on PDMS. (d,e) Fluorescence images of (d) CdSe/PCD-NH_2 and (e) PCD-NH_2 under blue excitation (top) and UV excitation (bottom). (f) Fluorescence emission

spectra of functionalized areas of (left) CdSe/PCD-NH_2 and (right) PCD-NH_2 with 488-nm excitation (yellow traces) and 405-nm excitation (blue traces); (g) PCD-NH_2 (top) PCD-NH_2 + RR (middle), and PCD-NH_2 + RR + CdSe (bottom), imaged with λ_{exc} = 561 nm, 10% laser power (left images), and with λ_{exc} = 488 nm, 50% laser power (right images) (h,i) Fluorescence spectra of RR/PCD-NH_2 and (i) RR+CdSe/PCD-NH_2 with λ_{exc} = 561 nm (orange traces) and 488 nm (green traces)..... 54

Figure 3.7 AFM images of alkyldiynamine monolayers (PCD-NH_2, top, and TCD-NH_2, bottom) on HOPG, with polymerization times specified on each image..... 62

Figure 3.8 Polymer lengths of TCD-NH_2 at early polymerization timepoints from the measurement of linear protrusions in AFM images..... 65

Figure 3.9 Polymer lengths of PCD-NH_2 at early polymerization timepoints from the measurement of linear protrusions in AFM images..... 66

Figure 3.10 Mean and standard deviation fluorescence values for regions of interest collected on TCD-NH_2/PDMS samples at the indicated polymerization timepoints..... 68

Figure 3.11 . Statistical analysis of fluorescence emission from TCD-NH_2/PDMS regions of interest analyzed at each timepoint..... 68

Figure 3.12 Mean and standard deviation fluorescence values for regions of interest collected on PCD-NH_2/PDMS samples at the indicated polymerization timepoints..... 69

Figure 3.13 . Statistical analysis of fluorescence emission from PCD-NH_2/PDMS regions of interest analyzed at each timepoint..... 69

ABSTRACT

Nature exhibits the power of chemical environment at nanoscale to efficiently regulate diverse processes on biological membranes, inspiring extensive applications of biotemplates on quantum computing to regenerative medicines. Approaches to design molecular-level chemical features often requires lattice structures of pristine inorganic surface to provide precise templates to routinely control placement of atoms, functional groups and molecules based on epitaxial assembly. However, emerging applications in biocompatible materials often involve in precise patterning on soft amorphous materials. The hetergeneties of such materials contribute significant challenges to express controllable nanoscopic features in a macroscopic scale. However, there is a great potential to leverage existed ordered chemical patterns to the nanoscopic functionalization of elastomers *via* crosslinking reactions.

Interfacial self-assembly provides a means of creating nm-resolution chemical patterns below the limitation of lithography. Particularly, long-chain functional alkanes generate lamellar phases through epitaxial alignment with inorganic substrates, forming 1-nm resolution functional stripes separated by ~5 nm of exposed alkyl chains. Diacetylene groups embedded in striped phases can undergo photopolymerization, forming conjugated π-bonds. An extensive polymer network on sPDA monolayer enhances the robustness of monolayers and provides reactive sites for crosslinking reactions, enabling the transfer of nm-precision patterns to amorphous materials, such as PDMS and acrylamide hydrogels. Scanning probe microscopy (SPM) has been typically used to understand on-surface polymerization of certain diacetylenes at molecular level on inorganic layered materials. It reveals different conformational change during polymerization on surface from in bulk crystals, but it is incapable of acquiring polymerization status at scales to incorporate observations in bulk. However, we utilized the reactivity of sPDA to transfer striped phases from inorganic substrates to soft elastomers via crosslinking. The transfer recovers the fluorescence of conjugated PDA networks, allowing optical characterization of striped phase monolayers at micrometer scales. We verified the correlation between fluorescence signals in macroscopic scales and polymerization studies by SPM. The combination of nanoscopic and macroscopic views assist us to discover significant impacts of subtle molecular structures on sPDA reactivity.

Polymerization of diacetylene, also known as topochemical reaction, was noticed by significant color change of bulk crystals. The reaction requires a delicate balance between angstrom-level movement and molecular arrangement, forming products with high molecular ordering. Studies of bulk PDA crystals have revealed the control of reaction efficiency by intermolecular interactions based on molecular structures. With the combination of SPM and fluorescence, we identified the importance roles of alkyl chain length and headgroups played in polymerization rate and efficiency. The interfacial polymerization exhibits similar reaction kinetics. However, due to the special "lifted" conformation of PDA evolved in interfacial polymerization, on-surface reaction is significantly sensitive to short-range interactions controlled by molecular structures.

Maximizing polymerization of striped phases benefit for the transfer reaction to elastomers, which have exhibited great potentials in development of electronic and biocompatible devices. Amine functionalities are useful in functional interface design, since primary amines are good nucleophiles for a wide range of reactions. Striped phases on elastomers with primary amines provide ordered reactive sites, and can serve either as functional handles for post functionalization of the surface for advanced purposes; Or other functions, including localized assembly of inorganic nanoparticles.

In this thesis, I present the studies of reactivity kinetics and efficiency of striped phases, depending on lengths of alkyl segments and headgroup chemistry. While fluorescence readouts offer the overall efficiencies of polymerization and elastomer transfer, SPM measurements reveal molecular details accounting for reactivity differences. Additionally, I demonstrate the utilization of striped phases primary amines on soft materials for post-functionalization and specific adsorption of nanocrystals, highlighting the versatile applications of this nm-scale chemistry boundary.

CHAPTER 1. INTRODUCTION

It is challenging to control nanoscopic chemical information on macroscopic scales, which benefits for a diverse range of applications in including quantum computing[1], energy conversion[2] and bioregenerative medicines.[3,4] However, biological membranes, constructed by amphiphiles, routinely organize the assembly of nanopatterns at μm-scale membrane interfaces.[5,6] Inspired by biology, our group translates the design principles of cell membranes into lying-down striped phase polydiacetylene (sPDA) amphiphiles on surfaces of layered materials (graphene, highly ordered pyrolytic graphite (HOPG) and MoS_2).[7,8] Assisted with polymerization, the formation of polydiacetylene enhances the robustness of lamellar structures and allows the crosslinking transfer of sPDA nanopatterns onto soft materials, such as polydimethylsiloxane (PDMS) and polyacrylamide hydrogels.[9] Here, I show that polymerization and crosslinking efficiencies of sub-10-nm striped phases are highly sensitive to intermolecular interactions (van der Waals interactions and hydrogen bonding) controlled by molecular structures of amphiphiles. Striped phases with primary amine functional groups on PDMS also present for post-functionalization and nanocrystal template, demonstrating the versatility of the nm-scale lamellar chemistry boundary in device design.

Precise control of atoms, functional groups and molecules at interface has been investigated intensively. Scanning probe replacement can manipulate surface moieties at sub-molecule level, but the method is limited in scaling potential.[10] Inversely, chemical lithography, such as microcontact printing[11], can generate patterns through macroscopic scale, but it is difficult to control chemical features below 100 nm. On the contrary, on-surface reactions provide a means of creating scalable high-resolution patterns.[12, 13] For example, functional alkanes align epitaxially with graphite lattice and form lying-down lamellar phase on the basal plane of layered materials. The striped patterns are composed by 1-nm functional group arrays, spaced with tunable ~5-nm alkyl segments present on surface, which can be characterized in detail with scanning probe microscopy (SPM).[14, 15] Stripe phases, embedded diacetylene groups, can undergo photopolymerization under UV irradiation forming polydiacetylene (PDA) backbones. The electronically conjugated structure of PDA has attracted research interests in molecular electronics.[16, 17] Thus, the polymerization was typically studied in low polymerization conversion.

However, the formation of continuous polydiacetylene network can stabilize nm-width arrays on surface, achieving broader goals of interfacial functionalization.

Our group has demonstrated that polymerized striped phase monolayers can regulate self-assembly of nanocrystals[18, 19] in organic solvents. Recently, we observed the crosslinking reactions between sPDA and crosslinkers in elastomers.[9] The covalent reaction results in the exfoliation of lamellar sPDA monolayers and covalently stabilizing the 10-nm orthogonal features remaining on a new elastomer surface. This type of reactions enables the transfer of high-resolution striped phases from inorganic layered materials to soft, amorphous materials, opening the possibilities for the design next-generation biocompatible devices. To maximize the benefits from sPDA chemistries on various substrates, it is crucial to understand the reactivity of PDA at desirable scales.

Polymerization of diacetylenes is a lattice controlled topochemical reaction.[20, 21] This solid-state polymerization of crystalline diacetylenes happens between C1 and C4 atoms of adjacent diacetylene moieties. Molecular structures determine the possibility and efficiency of the reaction by guaranteeing delicate balances of angstrom-level movement and molecular ordering in crystalline structures. Certain sPDAs on 2D materials has been studied by SPM at molecular levels. There are similar features in both sPDAs and bulk crystalline PDAs, such as the formation of ordered "blue" form with extended PDA and thermodynamically-favored fluorescent "red" form with disordered backbones.[17, 22, 23] However, sPDA monolayers, with long alkyl segment, generate lifted PDA backbones with flanking methylene groups out of surface plane in order to accommodate steric clashes of alkyl chains while maintain suitable bond angles.[15, 24, 15, 25] Although linear PDAs backbones are resolvable by SPM with low polymerization conversion, the prevalent angstrom-level protrusions add significant challenges for SPM imaging with high conversion due to the disruption of surface flatness. However, it is more challenging for SPM to resolve details in molecular level with scanning length above ~500 nm, which limits the understanding of polymerization comparable to studies of bulk system.

Optical characterizations are typically used for polymerization of crystalline diacetylenes because of the conjugated electronic structure, but it is not feasible for sPDA on HOPG because of its strong quenching effect on fluorescence. However, we recently reported the transfer of sPDA films to PDMS.[9] The transfer recovers the fluorescence of sPDAs with molecule-dependent emission intensity. In Chapter 1, we demonstrate that the fluorescence of transferred sPDAs can

serve as a macroscopic readout for polymerization, complementing information acquired from SPM at molecular level. With combined methods, we reveal a substantial difference in polymerization efficiencies between striped phases of two commercially available diynoic acids: 10,12-pentacosadiynoic acid (10,12-PCDA) and 10,12-tricosadiynoic acid (10,12-TCDA). With 2 methylene groups shorter in terminal alkyl chain, 10,12-TCDA, having a 10-carbon terminated segment, exhibits faster polymerization with more topographical protrusions in atomic force microscopy (AFM) measurement and brighter fluorescence in optical observation. The differences in reactivity further affect the wettability of monolayers and crosslinking efficiencies of elastomers transfer. Suggested by previous studies and our observation, sPDAs with 10-carbon terminated alkanes is at the cusp form lifted backbones during the surface polymerization. We propose that an acceleration of chain propagation benefit from the minimal activation energy of 10-carbon terminal segment for striped phase diynoic acids. The potential high mobility of 10-carbon terminal chain may also facilitate relaxation to the red-form PDA at high conversion, enhancing fluorescence emission of transferred films on PDMS. This study highlights the sensitivity of polymerization efficiency to the length of moveable alkyl segments of sPDA, offering a design principle for striped phases with high chemical reactivity.

Biological membranes routinely regulate reactions, transportation and signaling in nanoscale lipid microdomains(e.g. lipid rafts[26]). To achieve or even excel the properties of nature, there are increasing demands for high-resolution reactive functional patterning on biocompatible materials in the field of bioengineering, including soft robotics[27], microfluidics[28] and extracellular matrix.[29] Elastomers, such as PDMS, are widely applied to biocompatible devices and medicine design.[30] The amorphous nature of PDMS creates challenges to achieve nm-resolution ordering. Methods, such as optical lithography[31] and microcontact printing (μCP)[32], struggle to control patterning details below 100 nm. However, based on crosslinking of PDA-silane groups of PDMS, we achieved the transfer the sub-10 nm orthogonal patterns onto the amorphous surface, opening new opportunities to design surface chemistry on amorphous surface. In Chapter 2, we proposed a probabilistic model that relates the efficiency of crosslinking transfer to lengths of sPDA oligomers, based on the same molecular-macroscopic combined characterization. From calculations, the elongation of oligomer lengths enhances the probability of sPDA-PDMS surface transfer, in company with improved the reactivity of single-site hydrosilylation. We also continuously investigated the polymerization rates with dialkylamines in consideration of headgroup

interactions. Based on the fluorescence trend of transferred film on PDMS, we find that 10, 12-tricosadiynamine (TCD-NH_2), and 10, 12-pentasadiynamine (PCD-NH_2) exhibit similar polymerization rate at the macroscopic level, independent of the lengths of terminal segments. Due to the weak H-bonding of amine headgroups, it is the proximal segment to adjust the conformation for the formation of lifted backbones. Additionally, Dialkylamine striped phases integrate good nucleophilicity of amine functional groups and ordered alkyl chains. We leverage the dual chemistries to achieve post-functionalization of headgroups and specific adsorption of inorganic nanocrystals, constructing micropatterns with tunable fluorescence on PDMS surface. Overall, this chapter provides an insight for sub-nm patterning on amorphous surface and showcases the potentials of this type of nanopatterns for applications.

In summary, striped phases amphiphiles on elastomers present great potentials in flexible electronics and biocompatible devices. The fundamental understanding of the transfer reactions is not limited in providing essential guidelines to design high-resolution patterns, but also suggest detailed interactions to construct complex structures for versatile applications.

CHAPTER 2. DESIGN PRINCIPLES FOR ACCELERATING AN ON-SURFACE POLYMERIZATION, CHARACTERIZED FROM SINGLE-POLYMER TO MICROSCOPIC SCALES

A version of this chapter has been published in *Angew. Chem. Int. Ed.*.
DOI: 10.1002/anie.202110517

2.1 Introduction

Precisely controlling placement of atoms, functional groups, and molecules at interfaces is central to applications ranging from quantum computing[1, 33] to synthetic bioreceptor design for regenerative medicine.[4, 34] Scanning probe placement can be used to generate patterns with atomic precision, but is serial and thus has limited scaling potential and, in many cases, creates patterns with limited stability (e.g. at room temperature, in solvents). Conversely, lithographic chemical patterning (e.g. microcontact printing of alkanethiols on Au) is scalable, but controlling chemical feature precision becomes challenging at scales below 100 nm.

In contrast, on-surface reactions (e.g. boronic acid–diol condensation, coupling of thiophenes or diacetylenes, Ullmann coupling) [13, 35, 36] provide a means of stabilizing chemical patterns formed by interfacial assembly, and can often be characterized at the molecular level using scanning probe techniques. For instance, surface functionalization with striped phases of long-chain functional alkanes represents a means to routinely achieve 1-nm resolution functional patterns. Lamellar phases of substituted n-alkanes self-assemble epitaxially on materials such as highly ordered pyrolytic graphite (HOPG),[37-39] generating 1-nm-wide stripes of functional groups separated by ~5 nm of exposed alkyl chains, with stripe pitch tunable based on alkyl chain length.[40] Ordered striped phases incorporating a diacetylene in the alkyl chain undergo topochemical photopolymerization initiated by UV irradiation or electrons from an STM tip, forming a conjugated polydiacetylene (PDA) backbone (Figure 2.1, top left).[41-44] Most studies of this system have explored the electronic properties of individual PDAs with an interest in molecular electronics.[7, 24, 43]

Our group has demonstrated the stability (e.g. toward solution processing)[7, 45] and scalability (e.g. microcontact printing,[46] roll-to-roll transfer[47]) of these precision polymer layers, as well as their utility in controlling interactions with the environment (e.g. wettability, templating

nanocrystal assembly,[18, 48, 49] controlling biofouling and polyelectrolyte assembly[50]). Recently, we have also found that the striped PDA layer can be transferred to other materials using reactions (e.g. hydrosilylation) that link to the PDA backbone,[9] making it possible to perform high-resolution functional patterning of technologically important soft materials. Together, these findings point to the importance of understanding structure–function relationships for this class of on-surface reactions, to maximize utility in nm-resolution functional patterning.

The topochemical photopolymerization of diynes in bulk and in standing phase thin films,[20, 51, 52] has revealed a delicate balance between ordering and Ångström-scale dynamics underpinning these reactions. Ordering is required to minimize the distance between bond-forming carbons, maximizing chain propagation efficiency; however, changes in lattice parameter during the reaction must also be accommodated. With some monomers, the buildup of strain during reaction generates an autocatalytic process, leading to accelerated polymerization following an induction period. Optical measurements have established bulk polymerization kinetics, as well as conditions leading to conversion between the initially-formed extended (blue) and thermodynamically-favored twisted (red) forms of the PDA backbone. [21, 23, 53-54]

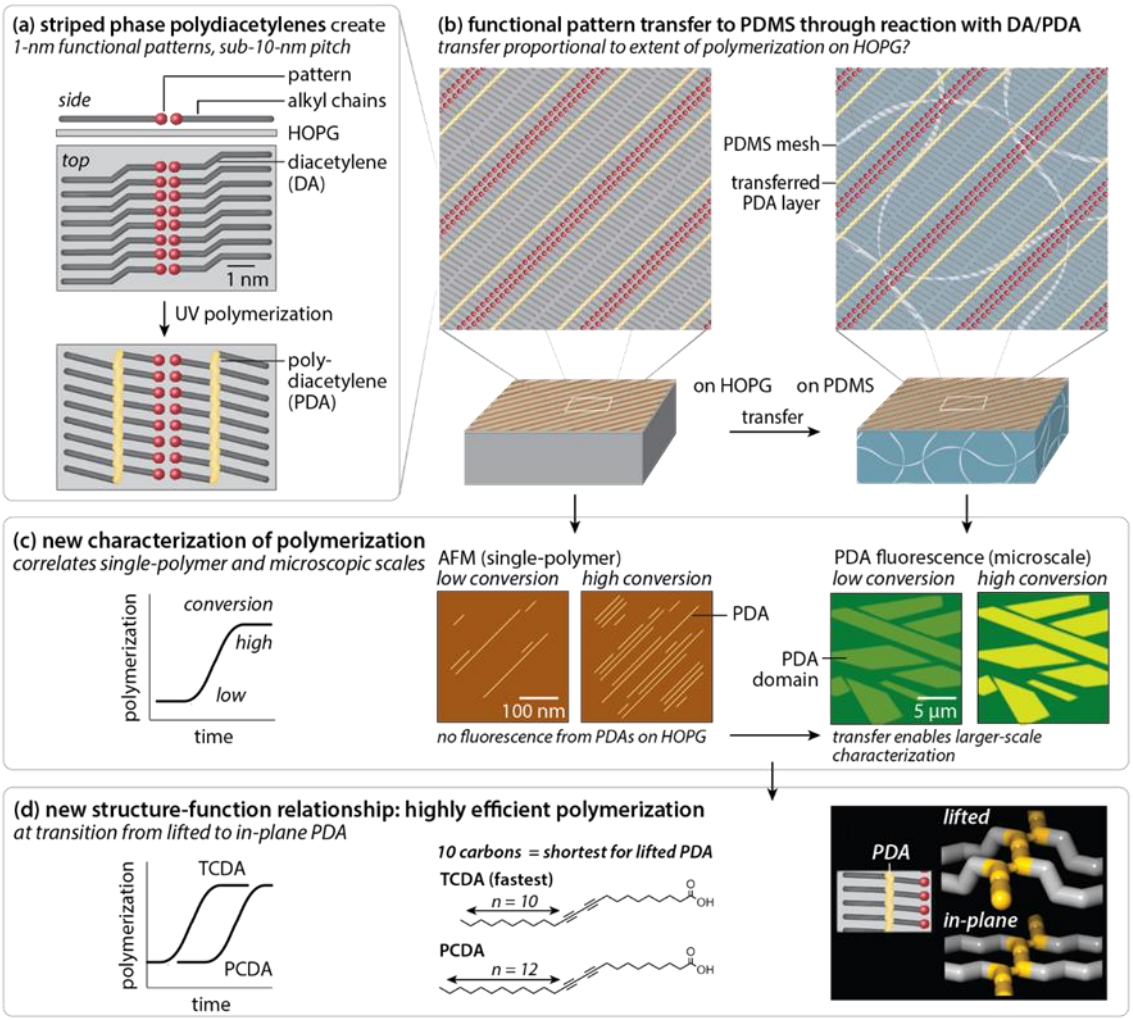

Figure 2.1 Schematics of (a) polymerization of a diacetylene striped phase on HOPG, and (b) of transfer to PDMS. Cartoon representation of (c) characterization of polymerization by AFM on HOPG, and by fluorescence on PDMS, and (d) of comparison between monomers

Polymerization of certain striped phase diacetylenes on 2D materials has also been studied at the molecular scale (via STM),[25, 36, 41-44,] revealing both similarities and striking differences with bulk PDA reactions. For instance, polymerization of pentacosadiynoic acid (10,12-PCDA) also typically produces an extended ('blue'-form) PDA. However, unlike the bulk reaction, the PDA backbone and flanking CH_2 groups lift slightly from the HOPG substrate (Figure 2.1, bottom right) to maintain suitable bond angles following rehybridization.7 Density functional theory calculations suggest that the lifted PDA is energetically slightly disfavored, relative to an in-plane PDA (Figure 2.1, bottom right), and likely forms due to steric clashes between long alkyl chain segments during polymerization.[15] For sufficiently short flanking alkyl chain segments, an in-plane

backbone is expected, more similar to conformations observed in bulk, but is more challenging to observe in scanning probe microscopy due to a lack of surface topographical features.[44]

2.2 Results and Discussion

2.2.1 Preparation of striped phase monolayer

Langmuir-Schaefer (LS) transfer was used to prepare striped monolayers, converting standing-phase amphiphiles at an air–water interface into lying-down phases on appropriate substrates (e.g. HOPG). For simplicity, we refer the names of diynoic acids in this chapter as PCDA and TCDA, unless they are compared with other monomers. Figure 2.2a show molecular models of unpolymerized and polymerized lamellar phases of PCDA. The lamellar width in energy-minimized molecular models (6.3 nm) coincides with periodic features observed in AFM images (Figure 2.2c); line scans (Figure 2.2c inset, acquired at white line in main image upper center) indicate topographic variations <0.1 nm. Following UV irradiation (λ_{max} = 254 nm), PDA backbones are observed (Figure 2.2b,d). The ~0.15-nm protrusions evident in AFM line scans (Figure 2.2d, inset) are consistent with the "lifted" PDA conformation for striped phases reported previously by Aono and coworkers.[15] Using protrusion features in AFM images, it is possible to quantify the number and length of polymers in nanoscopic areas of the surface. Scanning probe experiments have identified, for instance, that polymerization is initiated more readily on MoS_2,[42, 55] which has a lower adsorption enthalpy for alkyl chains, presenting lower energy barrier for alkyl chain reconfiguration during polymerization. Additionally, for hydroxyl-terminated molecules (with weaker interactions between headgroups), polymorphs with differences in alkyl chain orientation relative to the lamellar backbone can produce differences in polymerization rate. However, even in AFM images, which probe somewhat larger scales than STM, such features are difficult to quantify in images larger than 1 μm edge length. Therefore, it is difficult to extend this approach to examine surfaces polymerization at larger scales.

Previously, we have found that scanning electron microscopy (SEM) provides a complementary view of molecular ordering in these monolayers at larger scales.[46, 47] The monolayer scatters electrons more extensively than the conductive HOPG substrate, producing brighter features that contrast with darker unfunctionalized areas. Linear defects in the monolayer arise from lamellar narrowing during topochemical polymerization, and highlight the

directionality of molecular rows. In Figure 2.2e, multiple molecular domains are visible, oriented at angles of ~120°, characteristic of epitaxy with the hexagonal HOPG lattice. However, the SEM electron beam can contribute to DA polymerization, so it would not be straightforward to use SEM to assess extent of polymerization.

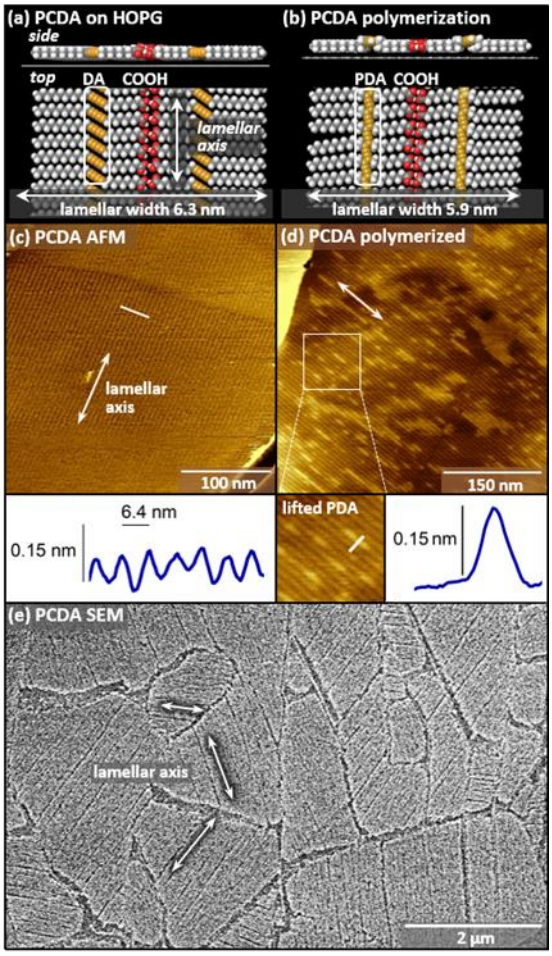

Figure 2.2 (a, b) Molecular models of unpolymerized and polymerized PCDA monolayers on HOPG (PCDA/HOPG); (c) AFM image of unpolymerized PCDA/HOPG; (d) AFM image of polymerized PCDA/HOPG showing "lifted" PDA; (e) SEM image of domain structure of polymerized PCDA/HOPG.

2.2.2 Measurements of striped phase PDA polymerization

Recently, our group reported fluorescence imaging of striped PDA monolayers transferred from HOPG to polydimethylsiloxane (PDMS) (Figure 2.3a). When PDMS is cured in contact with a PDA striped phase on HOPG, Pt-catalyzed crosslinking occurs between C–C multiple bonds in

the PDA and Si-H bonds in the PDMS crosslinker. Exfoliation of the PDMS from the HOPG then removes elements of the monolayer (polymers or potentially monomers, Figure 2.3b) that are linked to the PDMS polymer network. After transfer, fluorescence is visible from the transferred PDAs on PDMS, with domain morphology after transfer (Figure 2.3c) equivalent to the domain structures typically observed on HOPG (Figure 2.2e), consistent with transfer of intact PDAs to PDMS.

Transferred TCDA monolayers on PDMS (TCDA/PDMS) have emission maxima near 546 nm, with a series of C-C vibrational sidebands at longer wavelengths (Figure 2.3d). TCDA spectra are consistent with those of PCDA striped phases on PDMS (PCDA/PDMS, blue spectrum in bottom panel), which we have reported previously.[9]

Interestingly, although peak wavelengths are similar in spectra for PCDA/PDMS and TCDA/PDMS, the latter exhibits ~10-fold higher emission intensity, for monolayers polymerized and transferred under similar conditions (60-min UV photopolymerization, in Figure 2.3d, bottom). It would be reasonable to expect that emission intensity after transfer scales with the number of polymerized units generated in the monolayer on HOPG. A single covalent crosslink site should also be sufficient to exfoliate a much longer (and fluorescent) PDA (Figure 2.3b) while the transferred diacetylene monomers is non-fluorescent. Thus, the stronger fluorescence emission of TCDA/PDMS could indicate more extensive polymerization.

We examined whether fluorescence emission of monolayers on PDMS scaled with polymerization of monolayers on HOPG. We quantified polymerization events visible in (nanoscale) AFM images of TCDA/HOPG and PCDA/HOPG at timepoints up to 120 min, and compared these values with fluorescence emission intensities for the monolayers transferred to PDMS (Figure 2.3e).

Both TCDA and PCDA films exhibit an initial latency period, followed by a rapid increase in monomer-to-polymer conversion with increased UV exposure time (Figure 2.3e); such sigmoidal curves are characteristic of cooperative polymerization (autocatalytic effects) similar to those observed previously in bulk PDA crystals.[20] Calculated $t_{1/2}$ values based on AFM image analysis ($t_{1/2}$(TCDA/HOPG) = 35 min, $t_{1/2}$(PCDA/HOPG) = 78 min) illustrate more rapid polymerization of TCDA. Values calculated from fluorescence emission reveal a similar relationship ($t_{1/2}$(TCDA/PDMS) = 43 min, and $t_{1/2}$(PCDA/PDMS) = 66 min).

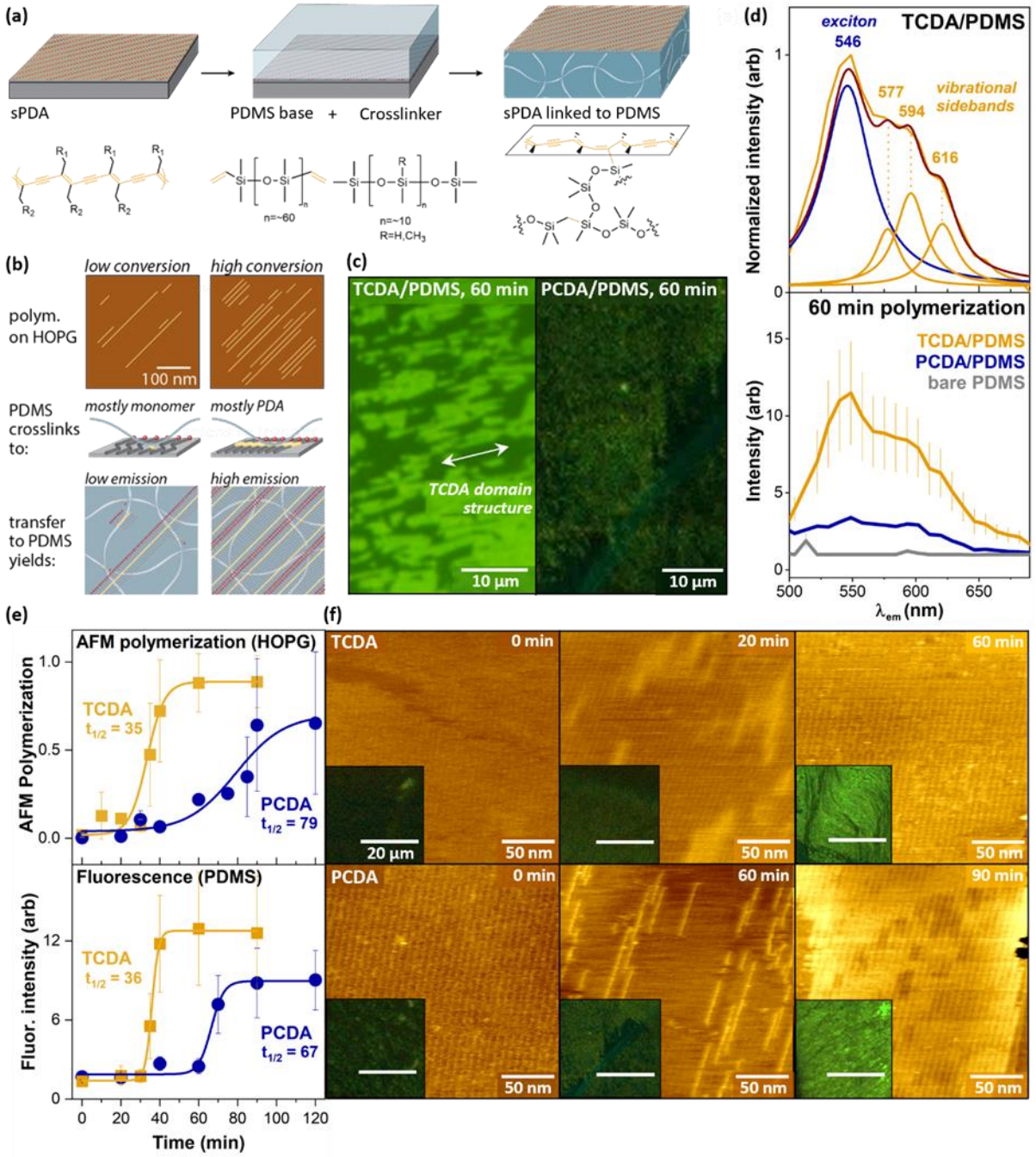

Figure 2.3 (a,b) Schematics of PDA transfer to PDMS; (c,d) Fluorescence (c) images and (d) emission spectra of striped TCDA and PCDA monolayers on PDMS; (e, f) Measurement of polymerization conversion by AFM (main image) and fluorescence microscopy (inset). Note that different timepoints are shown for TCDA (0, 20, 60 min) and PCDA (0, 60, 90 min) images, in order to illustrate similar conversion. AFM images are processed to the same color scale (full range = 1.8 nm), with the lower height areas of the monolayers set to equivalent height in each image. Scale bars in fluorescence insets are all 20 µm.

2.2.3 Impact of alkyl terminal segments on polymerization efficiency.

To understand design principles for efficient PDA reaction chemistry, we examined aspects of the polymerization mechanism that could lead to the observed differences in polymerization of PCDA and TCDA. Polymerization of diacetylenes proceeds through a diradical excited state, in which both ends of the growing polymer are reactive.[21] AFM images of both TCDA and PCDA exhibit lifted PDA backbones. Thus, it would be reasonable that excited state lifetimes are similar; in both cases, the reactive ends of the PDA are in similar physical environments, separated from the HOPG substrate. In that case, the observed difference in polymerization efficiency could relate to propagation rates, leading to differences in the average degree of polymerization (DP). We used AFM images acquired at similar degrees of conversion for PCDA and TCDA (e.g. Figure 2.4a,c and Figure 2.4 b,d). Because autocatalytic effects are in some cases associated with a higher DP during the rapid conversion phase, we compiled separate low-conversion and high-conversion histograms. Overall, the number average DP is higher for TCDA than for PCDA at both low and high conversion (Figure 2.4e), by a factor of ~1.5. Weight average DP values, which emphasize contributions from longer polymers, are 314 for high-conversion TCDA and 249 for low-conversion.

If the overall mechanics of the propagation step are similar for PCDA and TCDA, it is possible that that the difference in polymer length results from a lower activation energy for the TCDA propagation step, due to the shorter terminal chain. The ratio E_a(PCDA)/E_a(TCDA) coincides with the length ratio of the terminal chain segments (12 : 10 carbons), the observed difference in DP would be consistent with E_a(PCDA) = 0.09 eV and E_a(TCDA) = 0.08 eV for the propagation step. These values are comparable with activation energies for bulk PDA polymerization (e.g. 2,4-hexadiyne-1,6-diol bis(p-toluene sulfonate));[56, 57] thus, it may be reasonable that the more efficient polymerization of TCDA is contributed by a lower barrier to reconfiguration of the 10-carbon terminal chain segment during propagation.

Interestingly, although lifted PDA backbones are resolved with similar heights (~0.15 nm) for both TCDA/HOPG and PCDA/HOPG at low conversion (Figure 2.4a,c), image quality for TCDA/HOPG often deteriorates at higher conversion (Figure 2.4b). In contrast, PDA backbones in high-conversion PCDA/HOPG typically remain well-resolved (Figure 2.4d). STM studies have in some cases described streaky features in striped phases as tip-induced desorption events.[17, 22, 40] Given that we observe these features primarily for TCDA, which produces longer polymers and

has shorter anchoring alkyl chain segments, we examined the possibility that these features relate to strain buildup for longer polymers.

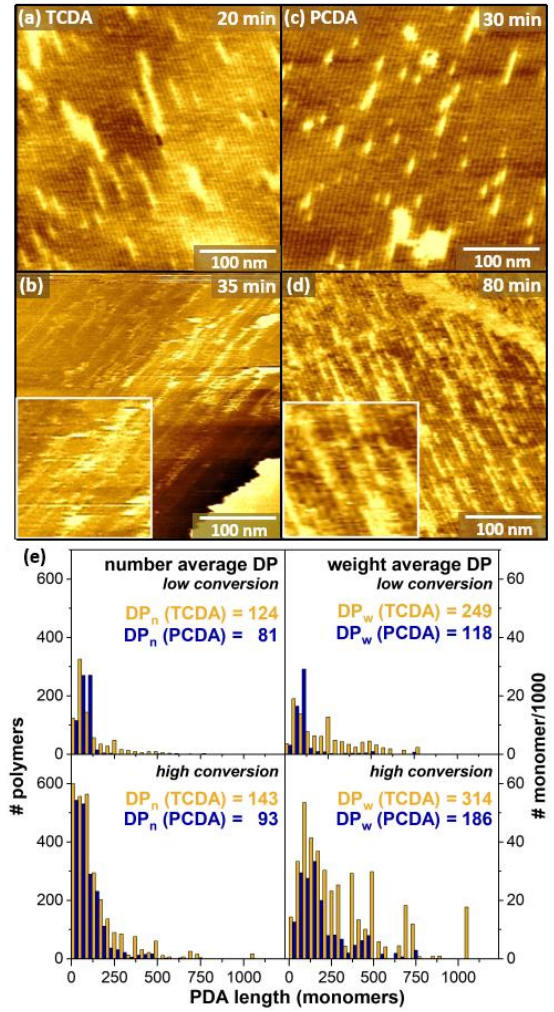

Figure 2.4 (a-d) AFM images of (a,b) TCDA/HOPG and (c,d) PCDA/HOPG at low (a, c) and high (b, d) conversion. (e) Histograms of number average and weight average degrees of polymerization at low and high conversion.

Molecular models of polymerization. We generated molecular models of PCDA and TCDA oligomers (Figure 2.5, see Experimental Methods for additional details). To mimic the structure of the reactive intermediate while allowing for energy minimization, hydrogens were added at the positions of the two radicals in the excited state. In the absence of explicit crowding, models illustrate a modest lattice mismatch for the PDA vs. the monomer, along the lamellar axis (4.75 Å repeat distance for the PDA, vs 4.70 Å monomer interchain distance observed

experimentally by STM[36]). Because it was not straightforward to create the very long oligomers observed experimentally (DP 80–300, Figure 2.4e), we simulated lattice mismatch by shifting a 12-mer and two of its flanking monomers (Figure 2.5a), in steps of 0.5 Å, the calculated lattice mismatch produced by the addition of 10 units to a polymer chain.

Models point to distinct fast and slow propagation directions for both PCDA and TCDA. At all steps, the active site on one end of the oligomer (top end, in Figure 2.5a) lies substantially closer to the bond-forming carbon in the next monomer, in comparison with the equivalent pair of atoms at the opposite end of the oligomer (Figure 2.5b). For displacements 2 Å and greater (modeling oligomers 40 units or longer), the distance between bond forming carbons is ~0.1 Å greater for PCDA than for TCDA. This would be expected to further increase differences in polymerization rates between the two molecules (in addition to differences in alkyl chain reconfiguration energy based on chain length).

Both models appear to accommodate a substantial amount of strain; at 4 Å offset, one end of the PCDA oligomer lifts onto the adjacent monomer, suggesting one possible mode for termination. At all steps, the TCDA polydiacetylene compresses to a greater extent than that for PCDA, but at ~4 Å offset, the entire backbone begins to tilt relative to the lamellar axis (Figure 2.5a, right), substantially increasing distances between bond-forming carbons at both ends, and illustrating another factor that may limit polymer length.

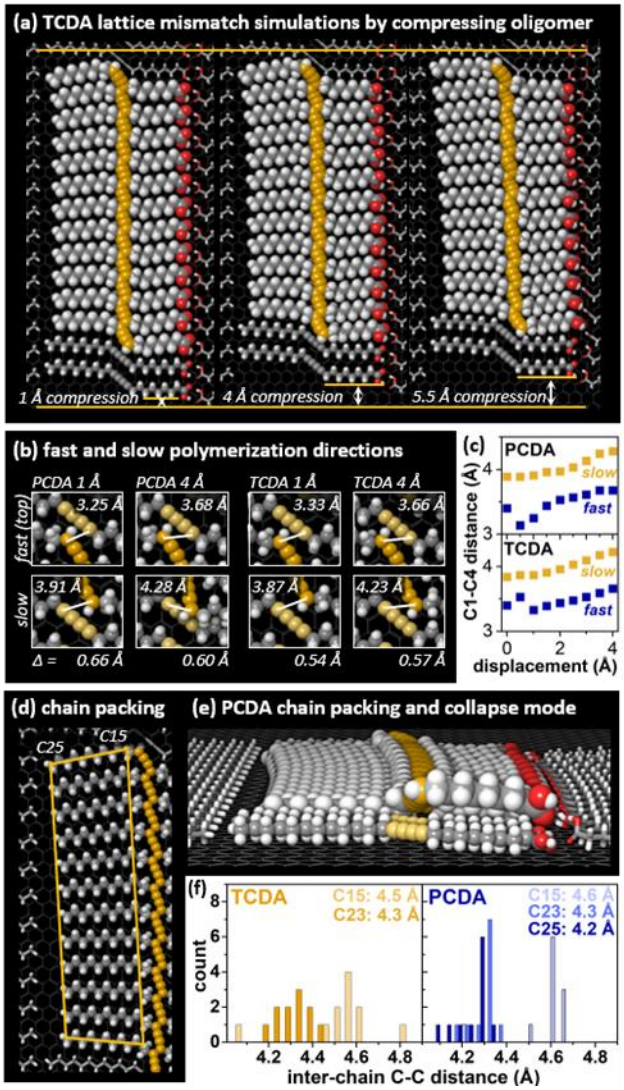

Figure 2.5 Molecular models of PCDA and TCDA polymerization. (a) Illustration of oligomer compression to simulate lattice mismatch. (b,c) Illustration and graph of differences in distances between bond-forming carbons at oligomer top and bottom. (d-f) Illustration of difference in alkyl chain packing distance near chain ends.

Models also illustrate factors likely to weaken alkyl chain ordering for polymerized TCDA, lowering the barrier to conversion to the twisted red-form PDA. The longer 4.75 Å PDA repeat distance increases distances between alkyl chains near the PDA, limiting stabilization through van der Waals interactions. Alkyl chain packing efficiency increases with distance from the PDA (Figure 2.5d–f), with mean interchain distances of 4.5–4.6 Å for C15 and values of 4.2–4.3 Å for C23-25. As a result, the shortest van der Waals interaction distances are at the chain ends, increasing stabilization associated with the extra two CH_2 groups in PCDA chains.[58] Overall, we

propose that the increased strain associated with longer TCDA polymers, in combination with the decreased stabilization provided by the shorter terminal chain segment, may result in strain release by conversion to the twisted red form of the PDA backbone.

2.2.4 Contact angle titrations of diynoic acid monolayers on HOPG

Alkyl chain disordering adequate to impact AFM resolution could, in principle, also impact wettability, an important gauge of macroscopic interface function. Contact angle titrations[59 60] were used to characterize the wettability of striped diynoic acid monolayers across the pH range from 2 to 13 (Figure 2.6). Here, we compared 10,12-PCDA, 10,12-TCDA, and two shorter-chain acids that form in-plane PDA backbones.

As we have observed previously for polymerized monolayers of 10,12-PCDA,[7 46] contact angles decrease at higher pH, as carboxylic acids are ionized to carboxylates and the surface becomes more hydrophilic (Figure 2.6, left panel). Differences in wettability with pH are more pronounced for the receding angle curves (round markers). The Young-Dupré model59 (used to calculate wettability of chemically heterogeneous surfaces) predicts lower contact angles for the shorter chains, due to the increased fraction of hydrophilic surface chemistry (headgroups) in the stripe. This expectation is borne out by the receding angle curves for 10,12-PCDA (blue traces in Figure 2.6, left panel), 10,12-heneicosadiynoic acid (10,12-HCDA, yellow), and 10,12-nonadecadiynoic acid (10,12-NDDA, green).

Consistent with the apparent alkyl chain disordering in AFM images, polymerized monolayers of 10,12-TCDA (red trace) were substantially more hydrophobic than those of the other diynoic acids. Differences were most pronounced at low pH values, at which carboxylic acid headgroups would be neutral, with ~10° increases in both advancing and receding contact angles for 10,12-TCDA compared with both 10,12-PCDA and 10,12-HCDA. Comparisons with contact angle titrations of unpolymerized monolayers (Figure 2.6, top right) indicate that this difference emerges during polymerization — pre-polymerization contact angles are similar for the four molecules.

To further test whether the accelerated polymerization and changes in surface wettability were associated with the 10-carbon terminal chain segment, we synthesized an additional amphiphile, 8,10-HCDA (Figure 2.6b). Similar to 10,12-TCDA, AFM images of 8,10-HCDA exhibit streakiness at relatively short polymerization times (Figure 2.6c). In contrast, AFM images

of 10,12-HCDA (8-carbon terminal chain segment, in-plane PDA backbone) after 20 min polymerization (Figure 2.6d) do not exhibit discernable topographical changes. Fluorescence intensity of 8,10-HCDA polymerized for 60 min then transferred to PDMS (Fig 2.6f) is greater than for 10,12-HCDA under the same conditions (Figure 2.6f); contrast enhancement for the 10,12-HCDA image reveals features consistent with PDA transfer, indicating that some polymerization does occur although the in-plane backbones do not produce contrast in the AFM image. Like 10,12-TCDA, monolayers of 8,10-HCDA exhibit polymerization-induced increases in hydrophobicity (Figure 2.6f), while 10,12-TCDA (an isomer of TCDA with an 8-carbon terminal chain segment, shown in red) does not.

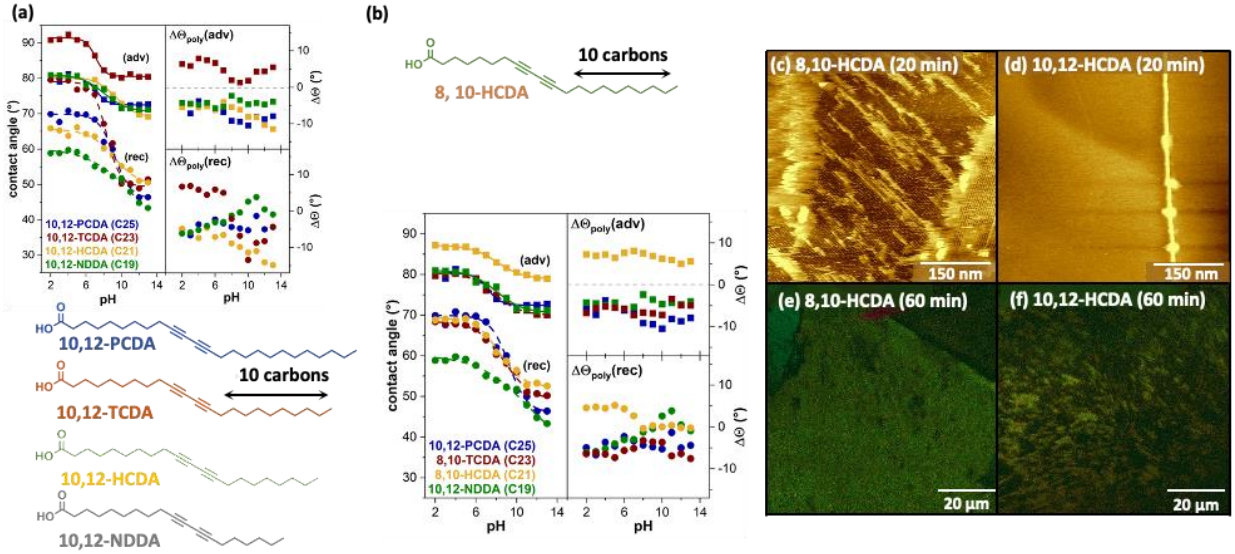

Figure 2.6 (a) Contact angle titration curves for polymerized 10,12-PCDA (blue), 10,12-TCDA (red), 10,12-HCDA (orange), and 10,12-NDDA (green). Difference between pre- and post-polymerization contact angles in advancing (top right) and receding (bottom right) measurements. (b) Structure of 8,10-HCDA and contact angle titration curves for polymerized 8,10-HCDA (gold), 10,12-PCDA (blue), 8,10-TCDA (red), and 10,12-NDDA (green). (c,d) AFM and (e,f) fluorescence images of (c,e) 8,10-HCDA and (d,f) 10,12-HCDA, illustrating more extensive polymerization of 8,10-HCDA at both timepoints. (f) Contact angle titration curves for polymerized 10,12-PCDA (blue), 8,10-TCDA (red), 8,10-HCDA (orange), and 10,12-NDDA (green). Difference between pre- and post-polymerization contact angles in advancing (top right) and receding (bottom right) measurements.

2.3 Conclusion

Striped phases of diacetylenes represent a potentially powerful means of routinely generating nm-resolution patterned functional interfaces, if the structure–function relations governing polymerization in the striped phase are better-understood. Here, using a combination of molecular-scale and microscale experiments, we show that two diynoic acids with 10-carbon terminal chain segments exhibit substantial acceleration in their polymerization compared with structurally similar diynoic acids with both longer and shorter terminal chain segments. Experiments also indicate that these molecules exhibit different impacts on wettability of 2D materials and reactive transfer to elastomers. We suggest that the 10-carbon terminal chain segment may generate this effect because: (1) it has adequate length to generate a lifted PDA backbone, physically separating the reactive moieties from the substrate, which may slow chain termination in comparison with shorter segments that produce an in-plane backbone, and (2) it has a minimal activation energy barrier to chain reconfiguration, in comparison with the longer chain segments that generate a lifted PDA, which may increase the rate of propagation, and may also facilitate relaxation to the red-form PDA at high conversion. Overall, the approach used here opens the possibility for a greater fundamental understanding of this class of on-surface polymerization reactions, on both molecular scales and on larger scales important for practical applications.

2.4 Experimental Methods

2.4.1 Materials

10,12-pentacosadiynoic acid (≥ 98 %), 10,12-tricosadiynoic acid (≥ 98 %) and chloroform (≥ 99.6%) were purchased from MilliporeSigma (St. Louis, MO). AFM probes, Bruker RFESP-75 (0.01−0.025 Ω·cm Antimony (n)-doped Si, nominal force constant 3 N/m and radius of curvature <12 nm) were purchased from Bruker AFM Probes (Camarillo, CA). Highly oriented pyrolytic graphite (HOPG) substrates, grade ZYB, were purchased from SPI Supplies (West Chester, PA). Milli-Q water (≥ 18.2 MΩ · cm resistivity) was used in all experiments. For simplicity, 10,12-pentacosadiynoic acid (PCDA) and 10,12-tricosadiynoic acid (TCDA), except in cases where they are being compared to other isomers.

2.4.2 Formation of striped phase monolayers via Langmuir-Schaefer transfer.

Striped phase diacetylene monolayers were prepared using a Langmuir-Schaefer conversion method: Langmuir-Schaefer transfer were performed on a microTrough XL Langmuir-Blodgett trough (Kibron Inc., Helsinki, Finland) with a customized temperature-controlled transfer stage reported previously [46]. HOPG substrates were cleaved immediately prior to sample deposition. The temperature of substrates was held at 35 °C; This temperature is low enough to avoid thermal polymerization of diacetylenes,[56] but high enough to avoid subphase condensation on the HOPG. For the deposition of diacetylenes (DAs), 34.5 µL of 0.75 mg/ml chloroform solution of the desired amphiphile was deposited on a subphase of deionized water (~ 18 MΩ · cm) as 1-µL droplets distributed across the trough surface. The system was allowed to equilibrate for 15 min prior to compression by sweeping the moveable barriers inward at 2.55 mm/min until the target mean molecular area (typically 30 $Å^2$/chain) was achieved. A freshly cleaved HOPG substrate mounted on the transfer stage was oriented nearly parallel to the air–water interface, and brought into contact with the subphase at a rate of 2 mm/min using the automated dipper. Following a 4-min period in contact with the subphase, the substrate was then lifted out of contact at the same rate, then blown dry with UHP N_2. DA monolayers were polymerized for the period of time stated in the manuscript (0 –120 min) by placing them under a hand-held UV lamp (λ_{max} = 254 nm, 8 W), with ~2 cm between the lamp and the substrate, to induce diacetylene photopolymerization. To ensure equivalent photon flux, flux was measured at several locations under the lamp, and samples were placed in locations with the equivalent flux.

2.4.3 Atomic force microscope (AFM) imaging and image processing

AFM imaging was carried out using a Veeco MultiMode with a Nanoscope V controller (Bruker Instruments, Billerica, MA) in tapping mode with Bruker RFESP-75 tips (nominal force constant 3 N/m and radius of curvature <12 nm) in an ambient environment. All images were processed with Gwyddion SPM software (http://gwyddion.net) prior to quantitative analysis. All raw data files were subjected to data leveling by mean plane subtraction and row alignment processing by fitting to median or median differences. Polymer counting and length measurements were performed using AFM images with resolvable lamellar features collected from 3 discrete

locations with sizes of 500 nm × 500 nm on HOPG. At least three HOPG substates were measured per polymerization condition. The following polymerization timepoints were analyzed:

0 min, 20 min, 30 min, 35 min, 40 min, 60 min, 90 min for TCDA;

0 min, 20 min, 30 min, 40 min, 60 min, 75 min, 85 min, 90 min, 120 min for PCDA.

Polymer identification, length and area measurements were performed using ImageJ (NIH, Bethesda, MD) software package, after setting the pixels/distance ratio.

2.4.4 Analysis of AFM images for assessment of polymerization on HOPG.

Features quantified in AFM images were utilized to estimate the monomer-to-polymer conversion at each polymerization timepoint. For individual PDAs, the number of polymerized monomers (degree of polymerization, DP) was calculated as the ratio of the length of the protruding feature in the AFM image, divided by the width of an individual monomer (~0.5 nm) in a striped PDA molecular row:

$$DP = \frac{polymer\ length}{0.5\ nm}$$

For polymerized blocks [insert graph], it was often not possible to individually resolve each PDA backbone in the AFM image, so the width of the block was used to estimate the number of contributing PDAs, based on the approximate width of a molecular row in molecular models:

$$N_i(block) = \left(\frac{PDA\ block\ width}{3\ nm}\right)$$

The total number of monomers (Nm) in an imaged area was calculated by dividing the imaged area by the monomer footprint (3 nm * 0.5 nm = 1.5 nm^2):

$$N_{m,init} = \frac{imaged\ area}{1.5\ nm^2}$$

The conversion ratio was then calculated as:

$$P(time) = \frac{\sum_i N_i DP_i}{N_{m,init}}$$

Features quantified in AFM images were utilized to estimate the monomer-to-polymer conversion at each polymerization timepoint. For individual PDAs, the number of polymerized monomers (degree of polymerization, DP) was calculated as the ratio of the length of the protruding feature in the AFM image, divided by the width of an individual monomer (~0.5 nm) in a striped PDA molecular row:

$$DP = \frac{polymer\ length}{0.5\ nm}$$

For polymerized blocks it was often not possible to individually resolve each PDA backbone in the AFM image, so the width of the block was used to estimate the number of contributing PDAs, based on the approximate width of a molecular row in molecular models:

$$N_i(block) = \left(\frac{PDA\ block\ width}{3\ nm}\right)$$

The total number of monomers (Nm) in an imaged area was calculated by dividing the imaged area by the monomer footprint (3 nm * 0.5 nm = 1.5 nm^2):

$$N_{m,init} = \frac{imaged\ area}{1.5\ nm^2}$$

The conversion ratio was then calculated as:

$$P(time) = \frac{\sum_i N_i DP_i}{N_{m,init}}$$

2.4.5 Scanning electron microscope (SEM) imaging

All scanning electron micrographs were acquired using a Teneo VolumeScope SEM (Thermo Fisher Scientific, Hillsboro, OR). Samples were mounted to standard SEM pin stub mounts with double-coated carbon conductive tape. To minimize surface charging during image acquisition, and to promote enhanced electrical contact between the sample and the specimen disk, PELCO colloidal silver was applied around the periphery of the HOPG substrate. High resolution imaging of striped phase PDA layers on HOPG was achieved using the in-column T3 (Trinity) detector in OptiPlan mode at working distances of 3.5–5.5 mm. Using a 32-µm aperture and 5.00 kV accelerating voltage, beam currents in the range of 0.4–2.0 nA produced the best resolution of the monolayers. Images were also process with Gwyddion SPM software for the presentation.

2.4.6 Confocal fluorescence microscopy and spectral imaging

Fluorescence images and emission spectra were acquired using a Zeiss LSM 880 Axio Examiner upright confocal microscope. Excitation was provided by a 488-nm Ar laser at 100 % power, focused through a 20x objective (plan-apochromatic, dry, NA = 0.80), with a 0.17-mm glass cover slip placed on the sample. Emitted light was detected by a 32-channel GaAsP spectral

photomultiplier detector with a pinhole size set to 1 Airy unit. Fluorescence images were collected at a resolution of 2856 × 718 pixels with 8-bit depth. Horizontal scans were acquired unidirectionally and averaged 16 times per line with a dwell time of 11.75 µs/pixel. Emission spectral data were collected from 495–691 nm (bin centered values) with 8.9-nm bin resolution.

2.4.7 Analysis of fluorescence at different timepoints

The fluorescence value for each timepoint was averaged by 15-30 regions from 3–6 samples. Fluorescence intensities were collected in each region of interest (ROI). If samples included regions of clearly different brightness in the in-focus area, we performed ROI analyses in each area to realistically capture sample variability. Each data set was analyzed using the quartile method to establish error bars and identify outliers if needed. Error bars graphed represent the interquartile region; that is, the lower end of the error bar represents the 25th percentile of the data values for that timepoint (Q1), and the upper end of the error bar represents the 75th percentile of the data values (Q3). This metric is robust toward outliers, but provides insight into skew in the distribution, if present. Quartiles calculated in this way were then used in identifying outliers. The interquartile range (IQR) is first calculated as Q3-Q1. Upper and lower bounds are calculated as follows: upper bound = Q3 + 1.5*IQR, lower bound = Q1 – 1.5*IQR. Data points lying outside the interval from lower to upper bound at each timepoint are identified as outliers and excluded from the calculated mean value (but are still included in the error bars).

0 min mean	0 min stdev	20 min mean	20 min stdev	40 min mean	40 min stdev	60 min mean	60 min stdev	70 min mean	70 min stdev	90 min mean	90 min stdev	120 min mean	120 min stdev
2.11	1.41	*3.13*	1.95	*3.97*	1.41	3.37	1.91	*25.80*	5.26	4.20	1.90	6.32	1.86
2.09	0.62	*3.30*	1.66	2.86	1.24	2.61	0.75	11.23	2.56	6.49	3.07	6.31	1.73
2.01	0.57	*3.13*	1.83	3.47	1.50	2.91	1.81	7.39	2.18	6.72	2.08	5.14	1.77
1.74	0.63	1.55	0.76	2.40	1.15	2.19	1.08	8.16	2.40	8.10	2.16	8.97	2.07
1.48	0.68	1.85	1.19	1.91	0.93	1.98	1.01	*23.22*	4.95	8.14	2.14	5.32	1.56
1.87	0.57	1.56	0.66	2.67	0.79	1.76	0.92	*20.39*	3.53	12.29	3.05	9.23	2.70
1.31	0.50	1.67	0.72	3.45	1.29	2.88	1.24	7.86	2.16	7.51	2.14	*18.02*	3.98
1.24	0.43	1.89	0.88	2.90	0.97	2.14	0.86	8.54	2.32	10.02	2.62	15.00	2.24
1.48	0.55	2.04	0.82	2.37	0.69	2.06	0.80	4.56	1.44	10.51	2.56	14.50	3.31
1.52	0.56	1.91	0.77	2.36	0.67	2.99	1.36	7.46	2.32	3.38	1.24	11.70	4.95
1.69	0.56	1.47	0.62	1.88	0.77	2.58	1.07	5.39	1.62	10.03	3.64	12.95	3.23
1.95	0.66	1.51	0.64	2.34	0.68	2.72	1.10	9.18	2.33	8.24	3.34	9.48	3.49
1.87	0.71	1.70	0.79	2.51	0.95	2.54	1.08	5.45	1.54	11.79	4.02	12.71	2.83
1.77	0.60	1.72	0.82	2.87	1.00	3.17	1.30	8.87	2.56	*24.75*	5.95	8.46	2.49
1.52	0.56	1.54	0.69	1.67	0.62	3.23	1.27	8.13	2.20	14.17	3.81	11.03	2.73
1.55	0.64	1.20	0.44	1.89	0.67	2.81	1.15	5.49	1.76	12.84	2.91	9.50	3.04
		1.24	0.49	1.82	0.62	3.54	1.41	1.92	0.82	6.12	2.66	8.30	2.77
		1.23	0.49	2.87	0.95	2.57	1.17	3.04	2.64	5.83	2.66	7.76	2.08
		1.41	0.56	3.33	1.16	2.91	1.47	6.55	2.20	8.85	3.52	8.58	2.37
		1.38	0.54	3.02	1.01	1.80	0.82	9.94	3.00	8.23	2.96	9.09	2.35
		1.41	0.56	2.96	0.97	2.27	1.03	9.04	2.76	9.53	3.50	9.41	3.02
				2.75	0.88	1.50	0.59	3.09	1.45	8.98	3.30	9.15	2.87
				3.04	1.09	*4.36*	3.04	7.12	2.45	6.26	2.63	8.99	2.65
						1.33	0.55	5.64	2.61	6.00	2.48	9.30	2.85
						2.02	0.66	5.15	3.25	8.46	4.08	7.98	2.57
						1.91	0.46	6.19	3.14	11.96	3.77	6.95	2.42
						2.04	0.76	3.84	1.82	12.26	4.81		
								7.20	2.77	10.09	3.63		
								6.65	2.61	4.20	1.90		
								8.17	2.87				

Figure 2.7 .Mean and standard deviation fluorescence values for regions of interest collected on PCDA/PDMS samples at the indicated polymerization timepoints. 15-30 regions were collected at each timepoint from 3–6 samples. Outliers identified through the quartile analysis are italicized.

	0 min	20 min	35 min	40 min	60 min	90 min
Int	**1.36**	**1.78**	**5.54**	**11.79**	**12.94**	**12.61**
std	0.24	0.74	2.46	3.69	4.30	4.32
std/int	0.18	0.42	0.45	0.31	0.33	0.34
Q1	**1.21**	**1.23**	**3.66**	**10.30**	**9.77**	**8.68**
Q3	**1.56**	**2.62**	**7.83**	**14.17**	**16.21**	**15.13**
IQR	0.35	1.39	4.18	3.87	6.44	6.45
lower bound	0.68	-0.85	-2.61	4.49	0.12	-0.99
upper bound	2.09	4.70	14.10	19.98	25.86	24.80

Figure 2.8 Statistical analysis of fluorescence emission from TCDA/PDMS regions of interest analyzed at each timepoint. In the manuscript, data are graphed with error bars representing the 25th percentile (Q1) and 75th percentile (Q3) of data values.

0 min mean	0 min stdev	20 min mean	20 min stdev	35 min mean	35 min stdev	40 min mean	40 min stdev	60 min mean	60 min stdev	90 min mean	90 min stdev
1.07	0.27	1.13	0.38	10.19	3.01	18.15	5.51	18.25	5.37	15.28	3.75
1.08	0.29	1.18	0.41	9.38	2.85	11.37	0.95	7.51	3.53	14.39	3.42
1.02	0.13	1.14	0.38	1.62	0.57	10.74	0.99	21.46	6.19	15.06	4.35
1.42	0.73	1.23	0.49	1.95	1.55	10.33	0.91	13.63	3.26	13.78	4.19
1.22	0.48	1.18	0.43	2.77	1.22	10.43	2.48	13.18	2.99	14.97	3.93
1.20	0.44	1.20	0.46	2.55	1.19	13.19	2.80	23.60	4.41	13.64	3.92
1.31	0.50	1.21	0.46	9.33	3.19	9.01	2.61	9.17	2.32	14.82	2.94
1.35	0.53	1.44	0.94	8.38	2.77	10.87	0.90	8.56	2.66	15.08	2.67
1.46	0.61	1.61	1.15	5.92	2.07	13.76	0.84	13.56	3.59	19.43	4.26
1.56	0.72	2.69	1.29	2.14	0.77	13.12	2.45	12.23	2.95	8.87	2.57
1.56	0.57	1.51	0.71	7.61	2.77	11.49	2.94	*38.44*	7.38	9.23	2.92
1.21	0.48	1.41	0.66	3.55	1.69	10.27	2.72	*27.17*	4.73	8.09	2.10
1.78	0.56	1.23	0.49	7.83	2.63	17.90	4.43	*43.13*	8.26	7.11	2.32
1.62	0.57	1.31	0.51	4.95	3.65	14.58	5.38	9.97	3.10	7.90	1.91
1.82	0.63	1.44	0.60	5.27	2.19	9.79	3.88	7.97	2.43	6.81	2.44
		1.44	0.58	5.76	2.30	17.91	3.13	11.54	3.46	8.11	4.07
		3.68	2.25	6.21	2.87	10.47	5.29	15.37	4.07	7.13	3.00
		2.87	1.91	2.83	1.12	4.97	1.79	13.44	4.01	19.25	5.78
		3.47	2.08	3.66	1.62	9.88	4.43	14.80	3.82	8.08	3.07
		6.35	1.78	4.30	1.66	17.77	5.38	11.96	5.00	12.10	4.27
		4.76	1.60	5.99	2.96	11.92	5.88	14.33	4.37	16.08	4.35
		9.12	2.65	5.39	2.58	12.46	5.60	11.30	2.85	10.26	4.43
		2.35	0.74	7.94	3.50	*20.07*	6.33	4.68	1.64	9.99	3.48
		1.88	0.52	8.68	3.05	13.10	5.50	8.40	2.57	15.35	6.08
		1.94	0.46	9.48	3.25	19.07	6.20	8.99	3.07	12.59	4.70
		2.47	0.72	5.84	2.22	4.56	2.21	15.75	6.51	16.86	5.01
		2.30	0.89	3.93	2.43	3.86	1.80	13.21	4.86	11.82	4.58
		2.60	0.77	5.08	2.95			17.57	6.05	16.25	4.24
				5.34	2.93						

Figure 2.9 Mean and standard deviation fluorescence values for regions of interest collected on TCDA/PDMS samples at the indicated polymerization timepoints. 15-30 regions were collected at each timepoint from 3–6 samples. Outliers identified through the quartile analysis are italicized.

	0 min	20 min	40 min	60 min	70 min	90 min	120 min
Int	1.69	1.63	2.68	2.49	7.18	8.82	9.04
Std	0.26	0.24	0.52	0.57	2.20	2.66	2.26
std/int	0.15	0.15	0.20	0.23	0.31	0.30	0.25
Q1	1.51	1.41	2.35	2.03	5.46	6.67	8.06
Q3	1.89	1.89	2.99	2.91	8.79	10.83	10.64
IQR	0.38	0.48	0.64	0.88	3.33	4.17	2.58
lower bound	0.93	0.69	1.39	0.71	0.46	0.41	4.19
upper bound	2.47	2.62	3.95	4.23	13.78	17.09	14.52

Figure 2.10 Statistical analysis of fluorescence emission from PCDA/PDMS regions of interest analyzed at each timepoint. In the manuscript, data are graphed with error bars representing the 25th percentile (Q1) and 75th percentile (Q3) of data values.

2.4.8 Molecular modeling

Software packages Maestro and Macromodel (Schrödinger, Cambridge, MA) were used for visualization of structures and energy minimization. All models were minimized using the OPLS3e force field with extended cutoffs for van der Waals, electrostatic and hydrogen bonding interactions. The Polak-Ribiere conjugate gradient (PRCG) algorithm was utilized for energy minimization with 50 000 maximum runs and 0.0005 kJ/mol-Å convergence threshold for the RMS gradient of the energy with respect to the coordinates. Models of PCDA and TCDA monolayers were assembled by generating 4 columns of 16 molecules each on a layer of graphene, with lateral spacings of 0.47 nm commensurate with previous STM observations by others, and with COOH groups paired at the model center. To maximize similarity of the starting points for the two systems, the TCDA monolayer was generated from the PCDA model by removing the terminal ethyl groups of PCDA monomers and shifting the outer rows inwards. The external two rows of molecules were used to provide reasonable constraints for the center two rows of molecules.

For molecular models of oligomer-monomer lattice mismatch, detailed procedures are described below: Models of PCDA and TCDA monolayers were assembled by generating 4 columns of 16 molecules each on a layer of graphene, with lateral spacings of 0.47 nm commensurate with previous STM observations by others,[36, 61] and with COOH groups paired at

the model center. To maximize similarity of the starting points for the two systems, the TCDA monolayer was generated from the PCDA model by removing the terminal ethyl groups of PCDA monomers and shifting the outer rows inwards. The external two rows of molecules were used to provide reasonable constraints for the center two rows of molecules.

To generate models of oligomer lattice mismatch used in 2.2.3 (Figures 2.5), in one of the center columns, 12 molecules were removed from the center of the row, leaving 2 molecules each at the row top and bottom. A pre-optimized 12-unit polymerized oligomer in the lifted backbone configuration (i.e. PDA and flanking methylenes 1.4 Å above the main plane of the monolayer) was placed in the vacancy. Monomers in the opposing row were adjusted slightly if needed to ensure H-bonded COOH dimer formation. The oligomer was minimized in the new configuration with all surrounding monomers frozen.

In the absence of constraints along the lamellar axis, the PDA backbone adopts a 0.475 nm repeat length (vs. 0.470 nm monomer periodicity observed in previous experiments by others [36, 61]). Experimentally, high conversion monolayers exhibited an average DP up to ~150 for TCDA, which would be difficult to model directly. Therefore, we generated a series of models in which we artificially induced conditions designed to mimic the compression of a very long oligomer with small mismatches in lattice parameter, in comparison with the unpolymerized monomer. In each model, the oligomer and the bottom two molecules in that row were shifted toward the top of the row in 0.5 Å steps (in principle equivalent to strain buildup from addition of 10 additional monomers to the polymer). After each step, the top and bottom pairs of monomers were frozen, as were the outer two rows of molecules. The oligomer and the facing row of molecules were allowed to adopt new configurations during minimization. Following completion of each minimization, the oligomer and two monomers were shifted another 0.5 Å.

For the PCDA model, this process was repeated 8 times, for a total 4 Å displacement. In optimization of the 8th model, one end of the oligomer rose over the adjacent monomer, which we took to be the endpoint of the displacement run. Figure 2.11 shows the initial PCDA oligomer model, and displacement steps 2, 4, and 8.

For the TCDA model, the 8th displacement step did not result in collapse of one end of the oligomer, so we performed three additional displacement steps, for a total end displacement of 5.5 Å. By the end of the 5.5 Å step, both ends of the oligomer were shifting in the plane of the monolayer to an extent that appeared to substantially lower the probability of additional

propagation steps, so this was taken to be the endpoint of the displacement run. Figure 2.12 shows the initial TCDA oligomer model, and displacement steps 2, 4, 8, and 11.

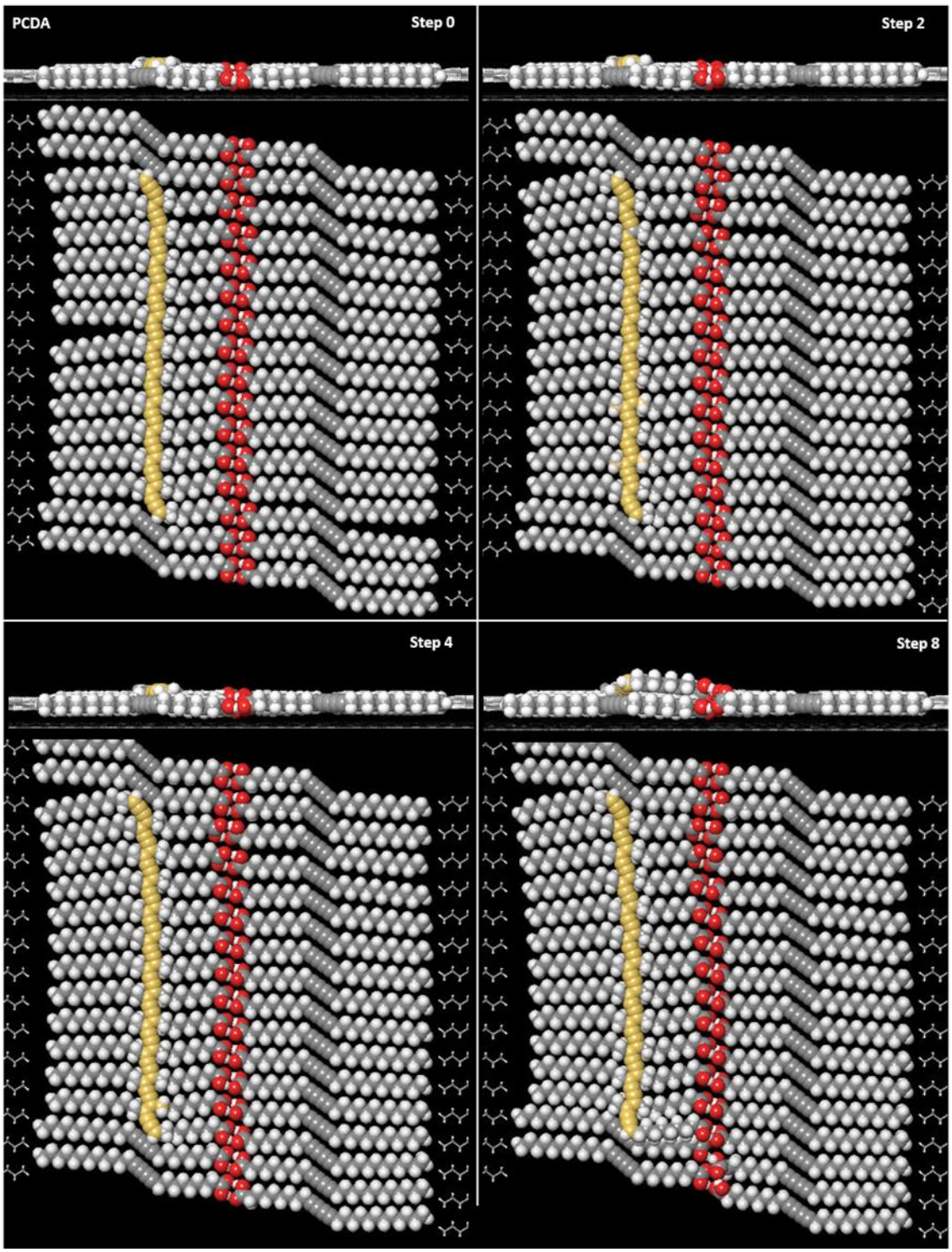

Figure 2.11 Energetically minimized PCDA models of initial state and displacement steps 2, 4 and 8.

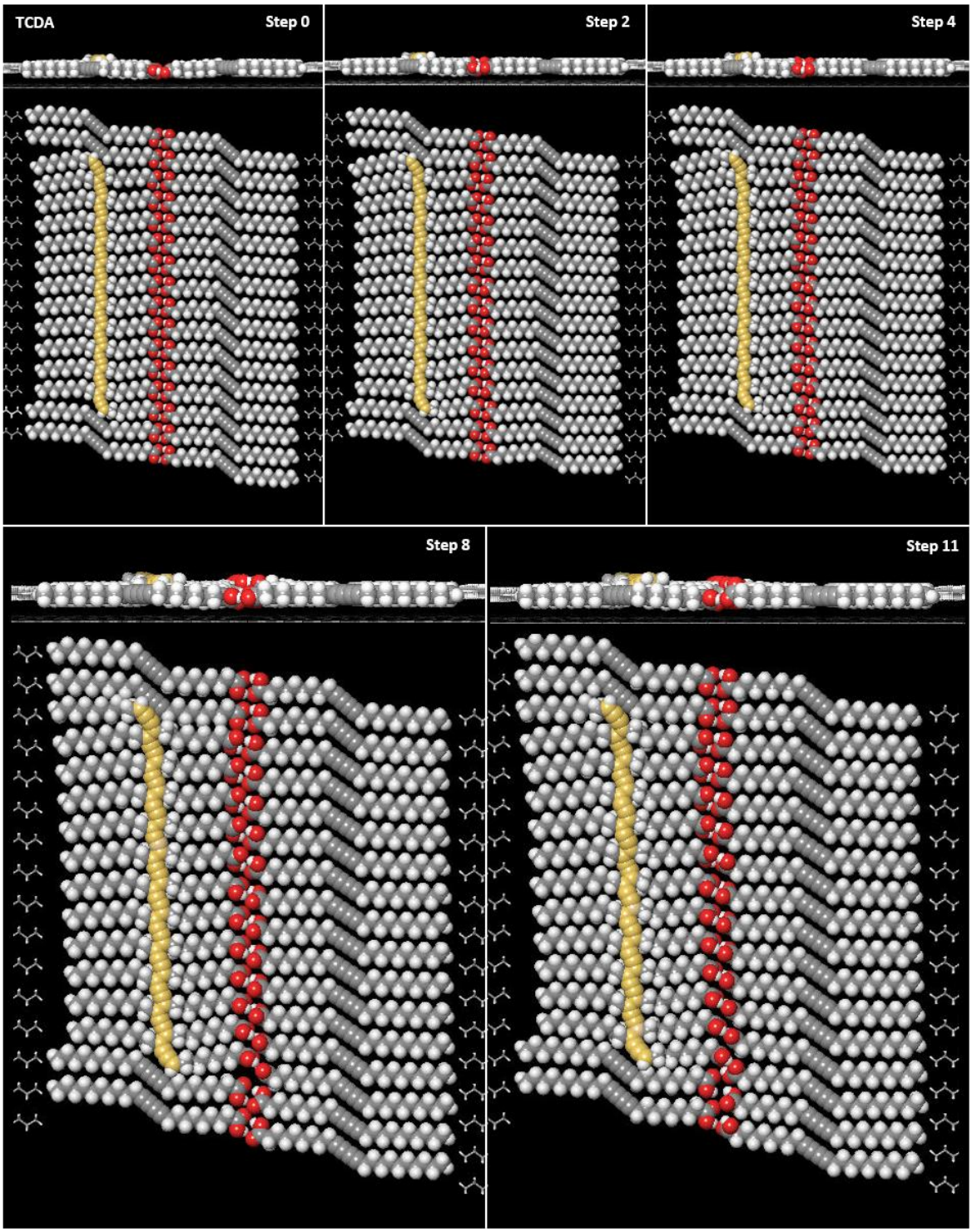

Figure 2.12 Energetically minimized TCDA models of initial state and displacement steps 2, 4, 8 and 11.

CHAPTER 3. POLYMERIZATION OF ALKYLDIYNAMINE STRIPED PHASES ON 2D MATERIALS: A ROUTE TO 1-NM-RESOLUTION REACTIVE FUNCTIONAL PATTERNS AT INTERFACES

3.1 Introduction

Materials with designed chemical environments near the atomic scale are important in areas ranging from electronics and quantum computing [1, 33] to regenerative medicine.[3] Approaches to designed molecular-scale chemical features at material interfaces have often relied on the lattice structure of a pristine inorganic surface to control placement of functional groups. [37-39, 55, 62] However, many emerging applications, including those in wearable electronics [63, 64] and regenerative medicine,[4] require chemical patterning of soft, amorphous surfaces. Such materials often express significant structural heterogeneties over length scales of tens to hundreds of nanometers, making it challenging to control molecular-scale placement on the surface.

Recently, we have demonstrated that it is possible to design nanometer-resolution chemical patterns on crystalline surfaces, [7, 55, 65] and transfer the sub-nanometer-thick surface layer to an amorphous substrate.[9, 50, 66] This approach allows us to pattern chemical structure an order of magnitude below the length scale of heterogeneity of the amorphous material. Our method takes advantage of an unusual striped-phase monolayer structure of amphiphiles that assembles noncovalently on highly oriented pyrolytic graphite (HOPG), graphene, and other 2D materials (e.g. MoS_2). In the striped phase, alkyl chains orient parallel to the substrate (Figure 3.1 a), forming 1-nm-wide rows of functional groups separated by ~5-nm-wide stripes of exposed alkyl chains.[17] Striped phases in which the monomers include an internal diacetylene can undergo UV photopolymerization, forming conjugated polydiacetylene (PDA) backbones.[41, 43, 44] Classically, such phases have been studied with an interest in molecular electronics, [16, 24] due to delocalization of electrons in the striped-phase PDA (sPDA). However, we have shown that it is also possible to use the sPDA backbone to tether together patterned functional groups for covalent transfer to materials such as polydimethylsiloxane (PDMS).[9]

The monolayer transfer process relies on efficient polymerization of the DA monolayer on the 2D substrate. Although there is a significant body of knowledge regarding DA polymerization in bulk,[20-21, 67-68] there is limited knowledge of the monomer structural features that maximize polymerization efficiency in striped phases. Such an understanding is not central to work aimed

molecular electronics, which typically takes advantage of individual, well-separated sPDAs to examine electronic structure. However, polymerization efficiency is critical for applications, including transfer to PDMS, that rely on high conversion to the sPDA. Recently, we have shown that there is a large difference in polymerization efficiency between the two commercially available diynoic acids most comdmonly used in striped phase assembly.[66] Differences in monomer alkyl chain structure appear to impact the rate of polymer propagation, leading to differences in polymer length.

Here, we extend understanding of sPDA polymerization and reactive transfer processes in two key ways. First, we examine the role of monomer headgroup H-bonding in polymerization, making comparisons between COOH headgroups (which form strong H-bond dimers between rows) and amines (which have weaker H-bonding). Amine functionalities are especially useful in functional interface design, since primary amines undergo a wide range of reactions,[69-71] allowing for elaboration of the interface chemistry. Overall, the weaker H-bonding between amine headgroups appears to support rapid polymerization. Second, we combine molecular-scale information regarding polymer lengths with microscopic information on extent of transfer, developing a model that relates the probability of sPDA transfer to polymer length. This provides physical insight into the efficiency of the interfacial reaction process that drives sPDA transfer.

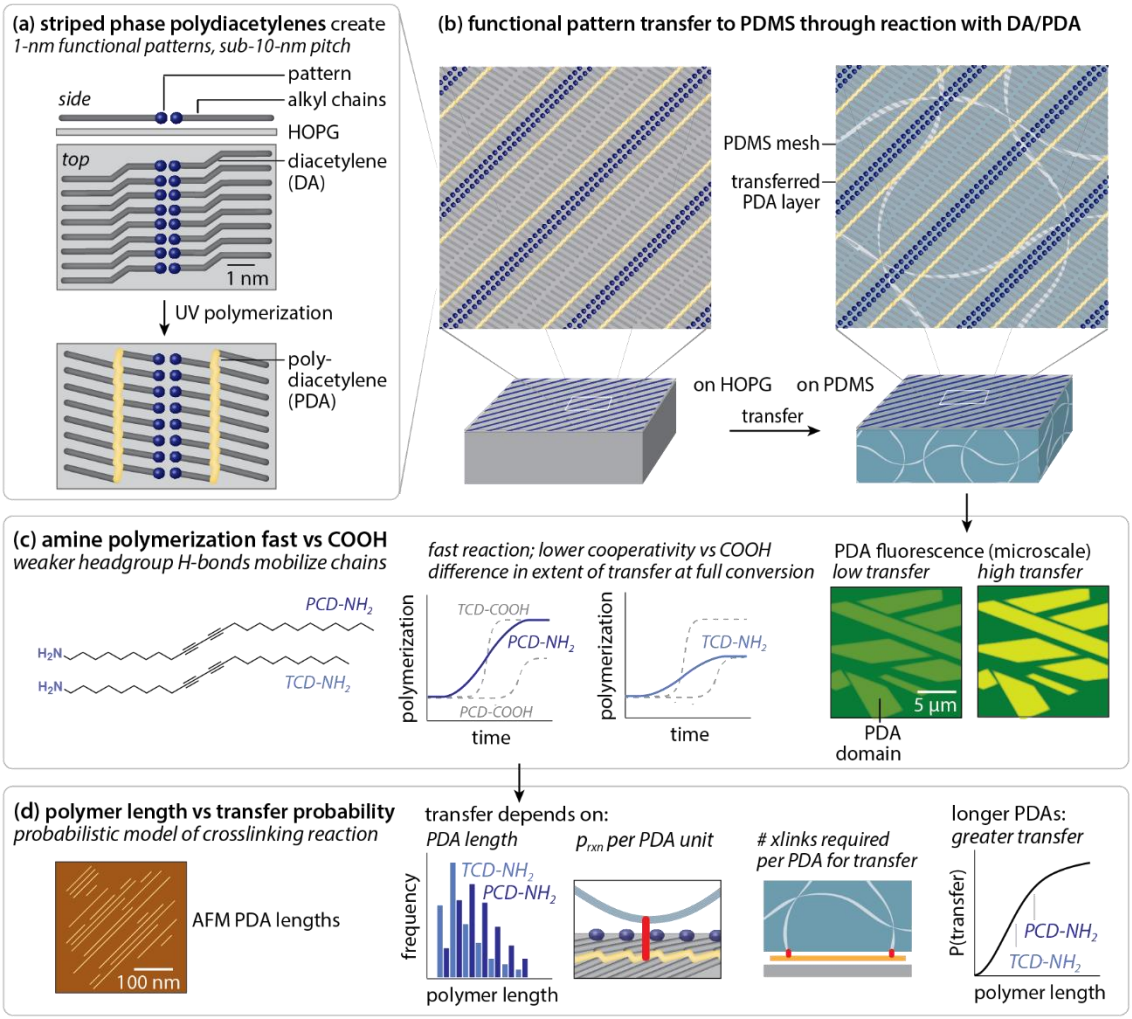

Figure 3.1 (a) Illustration of striped phase assembly on HOPG and (b) subsequent transfer of sPDAs to PDMS for nm-resolution functional patterning. (c) Illustration of use of fluorescence to characterize polymerization efficiency of NH_2 striped phases in comparison with COOH striped phases. (d) Illustration of probabilistic model for predicting sPDA transfer efficiency.

3.2 Results and Discussion

3.2.1 Preparation of striped phase monolayers

To compare polymerization efficiency of alkyl diynamines based on chain structure, we first prepared striped monolayers of 10,12-pentacosadiynamine (PCD-NH_2) and 10,12-tricosadiynamine (TCD-NH_2). Monolayers were assembled through Langmuir-Shaefer (LS) conversion, [65, 72] which reorders standing-phase molecules on an aqueous subphase into lying-down striped phases on highly ordered pyrolytic graphite (HOPG). Molecular models of unpolymerized (Figure 3.2a) and polymerized (Figure 3.2b) PCD-NH_2 after energy minimization

illustrate an edge-to-edge lamellar width ~6.5 nm. This is in reasonable agreement with the measured periodicity of the striped phase (~6.8 nm) in AFM images (Figure 3.2c, inset), which also includes the van der Waals distance between chain ends. PCD-NH_2 molecules (Figure 3.2c, main image) order epitaxially with the hexagonal HOPG lattice, exhibiting ~120^o angles between domains (lamellar axes in two domains labeled with white arrows). TCD-NH_2 assembles into similar domain structures.

Following UV irradiation, polymerized monolayers of PCD-NH_2 exhibit linear features (Figure 3.2d) with a 0.15-nm topographic protrusion (Figure 3.2d, inset). These features are consistent with the lifted form of the sPDA observed previously for polymerized lamellar phases of 10,12-pentacosadiynoic acid.[36] Similar structural features are also observed for TCD-NH_2.

SEM images (Figure 3.2e) enable characterization of monolayers on HOPG at scales similar to those in fluorescence microscopy images presented in later figures. Regions of bare HOPG appear darker, due to more limited secondary electron scattering; small defects in molecular domains produced during polymerization highlight molecular row orientation in large domains (highlighted in image).

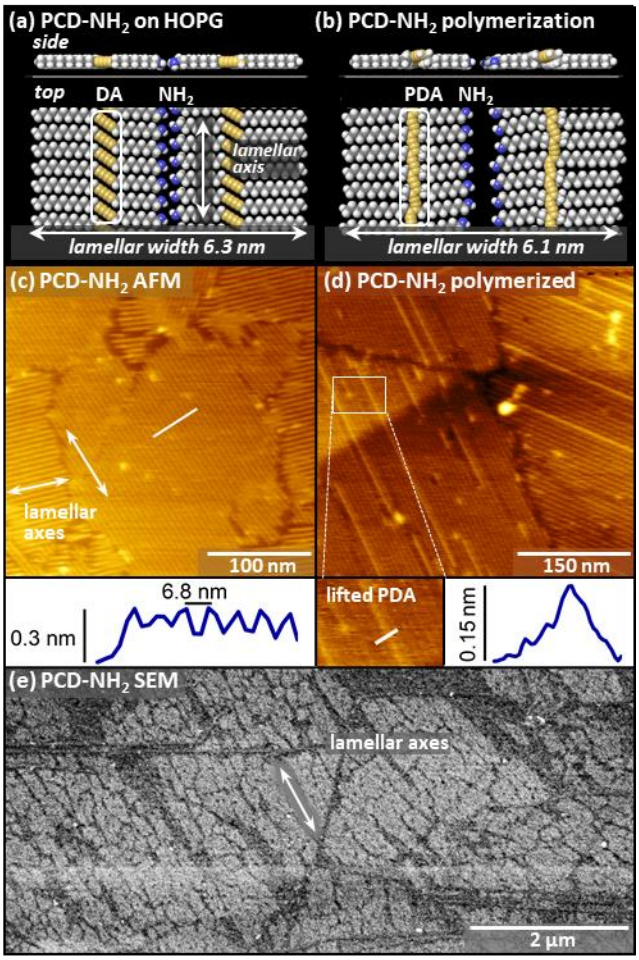

Figure 3.2 (a, b) Molecular models of (a) unpolymerized and (b) pol-ymerized PCD-NH_2 striped phases on HOPG, highlighting lamellar width. (c, d) AFM images of (c) unpolymerized and (d) polymerized PCD-NH_2. Arrows in (c) illustrate lameller axes in two domains oriented epitaxially with the HOPG lattice. Inset in (c) is a line scan acquired at the white line segment in (c). Inset in (d) illustrates topographic protrusion corresponding to 'lifted' sPDA backbone. (e) SEM image of PCD-NH_2 domains, showing lamellar axis revealed by cracks in monolayer.

3.2.2 Comparison of polymerization of TCD-NH_2 and PCD-NH_2.

To understand the impact of the amine headgroups on polymerization, we compared AFM and fluorescence images of polymerized TCD-NH_2 and PCD-NH_2. AFM images provide molecular-level insight into polymerization, including the lengths of individual polymers. Imaging fluorescence emission from the sPDA backbones provides a complementary ensemble view of the process. Although sPDA fluorescence is quenched on HOPG, we have recently found that polymerized lamellar phases can be transferred to non-quenching polydimethylsiloxane (PDMS).[9,

[50] We have also recently demonstrated that emission intensity on PDMS reflects the polymerization conversion on HOPG, for polymerized lamellar phases of diynoic acids.[66]

Monolayer transfer is carried out by curing PDMS in contact with an sPDA layer on HOPG. PDMS curing involves formation of covalent bonds between vinyl groups in the PDMS base polymer and Si-H groups in the crosslinker, in the presence of a transition metal catalyst. When carried out in contact with the sPDA layer, C-C multiple bonds in the sPDA can also participate in the reaction, covalently linking the sPDA to the PDMS network. When the PDMS is exfoliated from the HOPG, elements of the monolayer that are covalently linked to the PDMS are transferred from the HOPG. Fluorescence emission from sPDA backbones on PDMS, can be used to quantify the amount of sPDA transferred, providing a convenient means of estimating photopolymerization kinetics of the sPDA monolayer on HOPG.[66]

Here, we examined polymerization kinetics for amine striped phases on HOPG, preparing sets of TCD-NH_2/HOPG and PCD-NH_2/HOPG substrates, and controlling UV irradiation time in the range from 0–90 min. Both types of amine sPDA phases exhibit sigmoidal trends in fluorescence emission with increasing polymerization time. This observation is consistent with a cooperative polymerization process, in which strain increases due to differences between monomer and polymer unit cells produces accelerated polymerization later in the process. Cooperativity is common in bulk polymerization of PDAs,[20, 56] and is consistent with our previous observations of TCD-COOH and PCD-COOH sPDA reactions on HOPG.[66]

For sPDAs with COOH headgroups, monomers with 10-carbon terminal chain segments exhibited more rapid polymerization, in comparison with diynoic acids with shorter or longer terminal segments, meaning that TCD-COOH polymerizes much more rapidly than PCD-COOH, with a shorter $t_{1/2}$, and greater maximum fluorescence emission.

However, amine sPDA phases behave very differently. The midpoints of the sigmoidal curves collected here for amines are similar for the two molecules ($t_{1/2}$(PCD-NH_2) = 29.7 min, $t_{1/2}$(TCD-NH_2) = 33.0 min); both are similar to our previously observed $t_{1/2}$(TCD-COOH) = 36 min.[66] Additionally, at all points along the curve, PCD-NH_2 exhibits greater fluorescence emission, consistent with a greater amount of transferred PDA. Maximum fluorescence emission observed here for PCD-NH_2 is similar to that observed previously for TCD-COOH, while the maximum for TCD-NH_2 is similar to that for PCD-COOH.

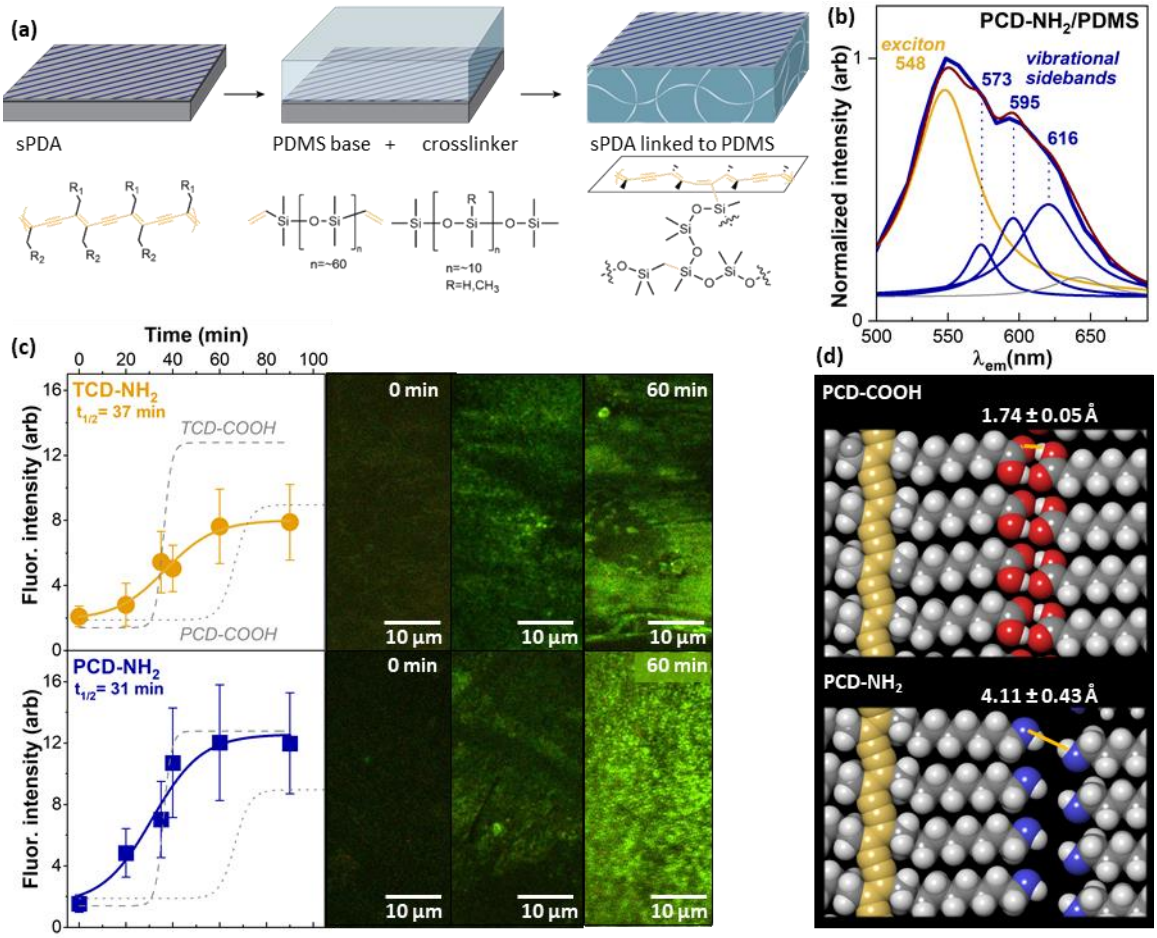

Figure 3.3 (a) Schematic of sPDA transfer to PDMS. (b) Fluorescence emission spectrum of PCD-NH_2/PDMS showing excitonic peak and vibrational sidebands. (c) Measurement of fluorescence emission for TCD-NH_2 and PCD-NH_2 transferred to PDMS following photopolymerization on HOPG for stated time; curve fits of previously measured values for structurally comparable carboxylic acids (TCD-COOH and PCD-COOH) are shown in dashed and dotted grey lines, respectively. Representative fluorescence images at selected timepoints (0, 35, 60 min) are also shown. (d) Molecular models of conformational change associated with polymerization of PCD-NH_2 (top) and PCD-COOH (bottom).

For COOH-sPDAs, strong hydrogen-bonded COOH dimers constrain the movement of the chain segment proximal to the headgroups during polymerization (Figure 3.3 d, bottom). Therefore, the terminal segment structure determines PDA conformation and polymerization efficiency. For diynamines, the weaker H-bonding between amine headgroups decreases interaction strength between proximal chain segments. Segmental interactions of proximal and terminal chain segments are calculated using the following values: $CH_2\cdots\pi$ (125 meV), $CH_2\cdots CH_2$(63 meV) and $NH_2\cdots NH_2$ (86 meV),[58, 72] resulting in segmental values of E_{prox} = 1.8 eV (for both PCD-NH_2

and TCD-NH_2), E_{term}(PCD-NH_2) = 2.3 eV and E_{term}(TCD-NH_2) = 1.9 eV. These suggests that, during polymerization, motion of the proximal chain segment (Figure 3.3d, bottom) is energetically favored by 0.5 eV for PCD-NH_2 and 0.1 eV for TCD-NH_2.

The slope of the vertical section of the sigmoidal curve is often used as a metric for cooperativity in topochemical polymerization of PDAs. For both PCD-NH_2 and TCD-NH_2, although the polymerization is rapid (in comparison to COOH sPDAs), the slope of the sigmoidal curve is notably lower, consistent with decreased cooperativity due to weaker H-bonding interactions between headgroups.

3.2.3 Impact of terminal segments on chain propagation.

Next, we used data from AFM images to examine possible contributions to the greater fluorescence emission intensity from PCD-NH_2 in comparison with TCD-NH_2. Since emission should scale with the number of transferred sPDA repeat units, the difference could arise from either a greater number density of polymers formed at each timepoint (higher initiation rate), and/or greater propagation lengths (longer polymers) resulting from each initiation event. Polymer lengths are typically most clearly resolved at early timepoints; thus, we used AFM images acquired prior to $t_{1/2}$ to compare polymer lengths and number densities (Figure 3.4).

Polymer lengths were quantified for both TCD-NH_2 and PCD-NH_2 (Figure 3.4c-d). Histograms of number average degree of polymerization (Figure 3.4c) are plotted based on measurements of > 650 polymers of each type; since the alkyl chain spacing along the polymer is ~0.45 nm/chain, a polymer 45 nm in length corresponds to a degree of polymerization (DP) of 100. Weight-average degree of polymerization (DP_w) is plotted using the total number of of polymerized monomers that appear in a polymer of that DP (values on the y-axis are divided by 1000). Average PCD-NH_2 propagation lengths are greater than those for TCD-NH_2. (DP_w(PCD-NH_2) = 271, DP_w(TCD-NH_2) = 174). Propagation lengths for the 25- and 23-carbon amine sPDAs reverse the trend observed for carboxylic acids, in which the shorter terminal chain segment result in longer average propagation lengths (DP_w(PCD-COOH) = 118, and DP_w(TCD-COOH) = 248) at low conversion. Overall, domain sizes for TCD-NH_2 are smaller than those for PCD-NH_2, consistent with lower ceilings on polymer length, although average lengths of molecular rows in ordered domains exceed average polymer lengths, suggesting that domain size itself is not the primary constraint on polymerization.

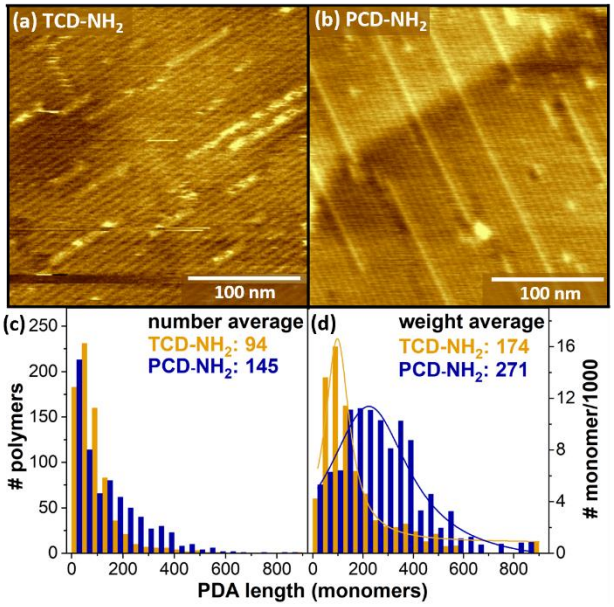

Figure 3.4 . (a, b) AFM images of polymerized (a) TCD-NH_2 and (b) PCD-NH_2 at low conversion timepoints; (c, d) Distribution of polymer lengths of PCD-NH_2 and TCD-NH_2.

3.2.4 Calculations of probability of sPDA transfer to PDMS based on PDA length

We considered the possibility that shorter polymer lengths (lower DP) for TCD-NH_2 may decrease the probability of transfer, consistent with the lower observed fluorescence emission on PDMS (I(TCD-NH_2) ≈ 0.6 * I(PCD-NH_2)). Overall, since the mesh (pore) size of SYLGARD-184 PDMS is ~10 nm, we suggest that the maximum number of crosslinks is < 1 per 20 PDA repeat units, since crosslinking must connect the sPDA to the main PDMS network (Figure 3.5a).

In Figure 3.5b, we used the polymer lengths measured for histograms in Figure 3.4 to predict fractional transfer of TCD-NH_2 and PCD-NH_2, based on a range of assumptions regarding the probability of PDMS crosslinking to each PDA unit (X-axis) and the number of PDMS–PDA crosslinks required for exfoliation of the sPDA (1 = blue trace, 2 = gold, 3 = red, 4 = green). Details of the analysis, including ranges chosen for P_{rxn} and the number of crosslinks required for transfer (n), are discussed in more detail in Experimental Methods

We then calculated the ratio of transfer predicted for TCD-NH_2 vs. PCD-NH_2 under each set of conditions. The horizontal grey line in Figure 3.5b (right) represents the experimentally observed ratio (~0.6). These calculations suggest that more than 1 crosslink total is required for sPDA exfoliation (n>1), since the single-crosslink criterion (n=1, blue trace) leads to higher TCD/PCD ratios than those observed experimentally, due to relatively high transfer efficiencies

for both molecules. Assuming only 2 crosslinks are required per sPDA transfer, the transfer ratio criterion suggests P_{rxn} = 0.07, while for n ≥ 3 or ≥ 4, P_{rxn} would be somewhat higher (0.014 or 0.021, respectively).

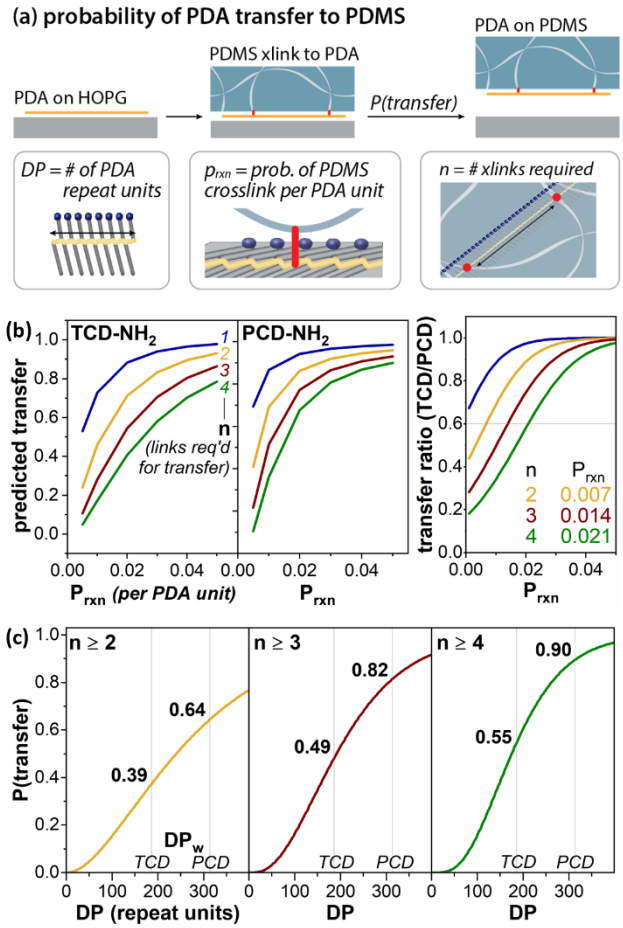

Figure 3.5 (a) Schematic illustrating structural factors predicted to impact transfer efficiency of sPDA transfer to PDMS. (b) Predicted transfer efficiencies for TCD-NH_2 and PCD-NH_2, within a selected range of per-subunit reaction probabilities (p_{rxn}) and number of crosslinks required for transfer (n). (c) Predicted ratio of TCD-NH_2 to PCD-NH_2 transfer. (d) Predicted fractional transfer vs number of sPDA repeat units, if at least 2 crosslink is required for transfer (left,gold), or if at least 3 (center, red) or 4 (right, green) crosslinks are required.

Figure 3.5c relates these values to predicted fraction of transfer for the average-length polymers of TCD-NH_2 and PCD-NH_2. If only 2 crosslinks are required for sPDA exfoliation (n ≥ 2, P_{rxn} = 0.007), the model predicts 39% transfer of average-length TCD-NH_2 polymers, and 64%

transfer of average-length PCD-NH_2 polymers. If at least 3 crosslinks are required ($n \geq 3$, $p_{rxn} = 0.014$), the predicted transfer increases to 49% (TCD-NH_2) and 82% (PCD-NH_2). Finally, if 4 or more crosslinks are required ($n \geq 4$, $P_{rxn} = 0.021$), the model predicts 55% (TCD-NH_2) and 90% (PCD-NH_2) transfer. Overall, we favor the hypothesis that our typical observations represent the $n \geq 2$ case (Figure 3.5c, left). Together, these experiments point to the potentially substantially role of large ordered molecular domains in transfer efficiency.

3.2.5 Applications of -NH_2 functional arrays on PDMS surfaces

One advantage to maximizing surface functionalization with amine striped phases is that primary amines are good nucleophiles, and can serve either as functional handles for post-functionalization of the interface, or in other functions including mediating assembly of inorganic nanocrystals.

Here, we examine the use of these surfaces to control adsorption of CdSe nanocrystals (Figure 3.6a). Nanocrystals are synthesized using previously reported procedures (see Experimental Methods) that produce crystals 2.6 ± 0.7 nm in diameter (Figure 3.6b,inset) with an octylamine ligand shell. Square patterns of striped phases of PCD-NH_2 on PDMS (Figure 3.6 c, e) were prepared by microcontact printing (μCP) striped phase PCD-NH_2 on HOPG, then transferring to PDMS (see Experimental Methods for more detailed descriptions of each step).

Prior to nanocrystal exposure, square patterns are visible in AFM phase images (Figure 3.6e) and in fluorescence emission with excitation in the blue range (440–460 nm) (Figure 3.6e top). No emission is visible with excitation in the UV range (330–350 nm) (Figure 3.6e, bottom). Following exposure to solutions of CdSe NC in cyclohexane, increased phase contrast is visible in AFM images (Figure 3.6c, top); modest changes in surface topography are also observed (Figure 3.6c, top inset), though these are irregular as the nanocrystals are not large relative to PDMS pore sizes. Stronger fluorescence emission is visible under both blue and UV excitation (Figure 3.6d top and bottom, respectively). Spectral imaging (Figure 3.6f) illustrates an ~10x increase in integrated emission intensity with both 488-nm and 405-nm excitation (green and blue traces, respectively).

Spectral emission intensities of μCP-patterned PCD-NH_2 (Figure 3.6e, ~2 a.u. at full conversion) are noticeably lower than those from PCD-NH_2 sPDAs prepared by LS transfer (Figure 3.3c, bottom, ~12 a.u. at full conversion), which is reasonable, given the smaller domain structures typically observed in microcontact printing. If transfer is consistent with the model developed in Figure 3.5, this would correspond to ~10 % transfer of the sPDA layer, and a DP_w ~100. Ongoing work examines strategies for increasing transfer for shorter sPDAs by increasing P_{rxn}.

To demonstrate the multifunctional nature of these surfaces, we then examined the capability for the surfaces to template sequential rounds of chemical patterning. We first covalently functionalized square patterns of PCD-NH_2 with rhodamine red (RR) succinimidyl ester, and subsequently with CdSe nanocrystals passivated with alkyl ligands (see Experimental Methods). Fluorescence images of bare PCD-NH_2 (Figure 3.6g, top), PCD-NH_2+RR (Figure 3.6g, middle), and PCD-NH_2+RR+CdSe (Figure 3.6g, bottom) were acquired at a wavelength chosen to excite RR (λ_{exc} = 561 nm, 10% laser power, left images) and at a wavelength chosen to excite the CdSe nanocrystals (λ_{exc}=488 nm, 50% laser power, right images). In images of bare PCD-NH_2, square patterns are not visible at the RR excitation conditions, even with contrast enhancement. Squares of PCD-NH_2 are weakly visible under CdSe excitation conditions, which use the same excitation wavelength as that for sPDA imaging (488 nm), although at lower power (50% vs 100%).

Following reaction with RR, square patterns are visible under 561-nm excitation (Figure 6g middle, left), while contrast is only modestly increased at 488 nm (Figure 6g middle, right). Significant background fluorescence is observed at 561 nm, even after vigorous washing, consistent with some diffusion of RR into PDMS pores. After further exposure to CdSe, similar contrast is observed at 561 nm (potentially with decreased background fluorescence), while emission at 488 nm increases. The diameter of CdSe NCs with their alkyl ligand shells is similar to PDMS pore diameters (~10 nm), consistent with the lower levels of background fluorescence observed at 488 nm following CdSe exposure, in comparison with background at 561 nm following RR functionalization.

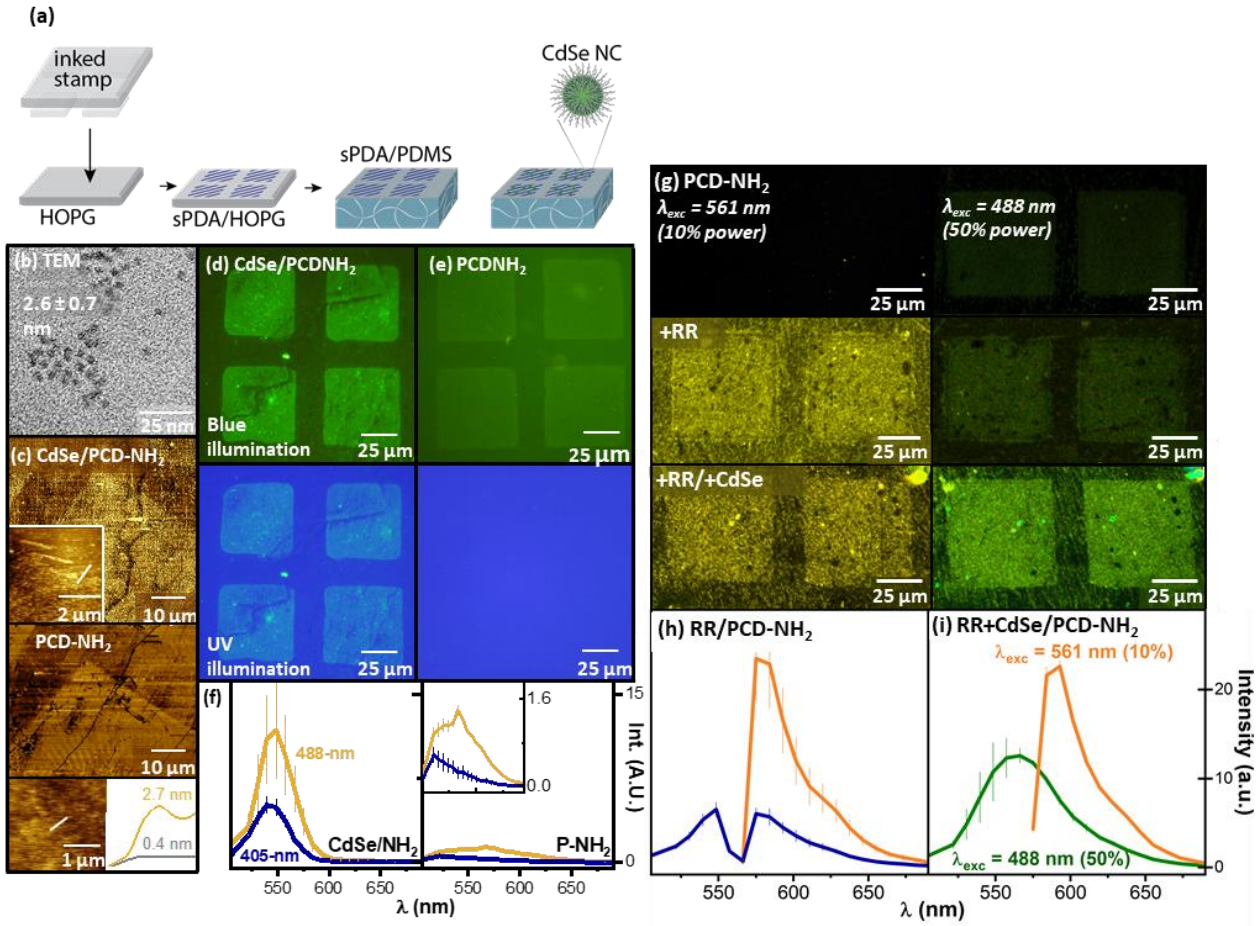

Figure 3.6 (a) Schematic of nanocrystal binding to striped PCD-NH_2/PDMS. (b) TEM image of CdSe nanocrystals used in adsorption experiment. (c) AFM phase images of (bottom) (top) CdSe/PCD-NH_2 and PCD-NH_2 on PDMS. (d,e) Fluorescence images of (d) CdSe/PCD-NH_2 and (e) PCD-NH_2 under blue excitation (top) and UV excitation (bottom). (f) Fluorescence emission spectra of functionalized areas of (left) CdSe/PCD-NH_2 and (right) PCD-NH_2 with 488-nm excitation (yellow traces) and 405-nm excitation (blue traces); (g) PCD-NH_2 (top) PCD-NH_2 + RR (middle), and PCD-NH_2 + RR + CdSe (bottom), imaged with λ_{exc} = 561 nm, 10% laser power (left images), and with λ_{exc} = 488 nm, 50% laser power (right images) (h,i) Fluorescence spectra of RR/PCD-NH_2 and (i) RR+CdSe/PCD-NH_2 with λ_{exc} = 561 nm (orange traces) and 488 nm (green traces).

3.3 Conclusion

Here, we have examined the polymerization and transfer of 1-nm-resolution patterns of alkylamines to the surface of PDMS. Using a combination of single-polymer and microscopic measurements, we quantify relationships between PDA length and transfer to PDMS, establishing approximate bounds on reaction efficiency and the number of PDMS–sPDA linkages required for transfer. Following transfer, we illustrate that such patterns can be used to promote both covalent

functionalization with fluorescent dyes and adsorption of CdSe nanocrystals with alkyl ligand shells. Overall, our findings here establish criteria for polymer lengths that lead to effective nm-resolution patterning of PDMS, and suggest that both alkyl chains and polar headgroups can play important roles in controlling adsorption to the PDMS surface.

3.4 Experimental Methods

3.4.1 Materials

10,12-pentacosadiynoic acid (≥98 %), 10,12-tricosadiynoic acid (≥98 %), Jones reagent (2M in aq. H_2SO_4), 10-undecynoic acid (95 %), 1-tetradecyne (97 %), 1-decyne (98 %), 1-octyne (97 %), iodine (99.8 %), N-bromosuccinimide (≥99 %), tetrahydrofuran (≥99.9 %), copper chloride (99.5 %), copper(I) iodide (98 %), silver nitrate (≥99.0 %), morpholine (99 %), hydroxylamine hydrochloride (98 % and 99.999 %), ethylamine solution (66.0–72.0 % in H_2O), sulfuric acid (95.0–98.0 %), sodium thiosulfate, sodium bicarbonate, and anhydrous sodium sulfate (≥99.0 % purity), cadmium oxide (CdO, 99.99 % trace metals basis), selenium (100 mesh, ≥99.5% trace metals basis), trioctylphosphine oxide (TOPO, 99 %), trioctylphosphine (TOP) (technical grade, 90 %), were all purchased from MilliporeSigma (St. Louis, MO) and used as received. n-Octadecylphosphonic acid (ODPA, 97 %) was purchased from Alfa Aesar (Ward Hill, MA). 1-Dodecyne (98 %) was purchased from ACROS Organics (Fair Lawn, NJ). Rhodamine Red-X succinimidyl ester and solvents, including acetone (>99.5 %), methanol (>99.5 %), ethyl acetate (>99.5 %), diethyl ether (anhydrous), hexanes and toluene were purchased from Fisher Scientific (Hampton, NH) and used as received. Non-8-yn-1-ol (97 %) was purchased from MilliporeSigma (St. Louis, MO), and used as received. Potassium hydroxide and heptane (99.0 %) were purchased from Fisher Scientific (Hampton, NH) and MilliporeSigma (St. Louis, MO), respectively. Silica gel was purchased from Macherey-Nagel (Bethlehem, PA) and used as received. AFM probes, Bruker RFESP-75 (0.01–0.025 Ω·cm Antimony (n)-doped Si, nominal force constant 3 N/m and radius of curvature <12 nm) were purchased from Bruker AFM Probes (Camarillo, CA). Highly oriented pyrolytic graphite (HOPG) substrates, grade ZYB, were purchased from SPI Supplies (West Chester, PA). 25-mm PTFE syringe filters were acquired from

VWR (Radnor, PA). Milli-Q water (≥ 18.2 MΩ · cm resistivity) was used in all experiments where water was required.

3.4.2 Langmuir-Schaefer transfer to generate striped alkyldiynamine films

Striped phase alkyldiynamine films were prepared using a temperature-controlled Langmuir-Schaefer conversion method reported previously,[9, 66] and described briefly here. Langmuir-Schaefer transfers were performed on a microTrough XL Langmuir-Blodgett trough (Kibron Inc., Helsinki, Finland) with a customized temperature-controlled magnetic transfer stage reported previously.[73] HOPG substrates were glued to stainless-steel AFM specimen discs. For each transfer, the HOPG on the specimen disc was mounted on the temperature-controlled transfer stage, immediately following HOPG cleavage. The temperature of substrates was held at 30 °C to avoid subphase condensation and thermal polymerization of the alkyldiynamines on HOPG. 20 µL of 0.50 mg/mL of the desired alkyldiynamine in $CHCl_3$ was deposited in evenly distributed 1 µL droplets on a subphase comprised of 40 mM $CaCl_2$ in milli-Q water at 30 °C. The system was allowed to equilibrate and to evaporate the $CHCl_3$ carrier solvent for 15 min. Compression of the subphase was carried out by sweeping the trough barriers inwards at a rate of 5 mm/min from an area of 20500 mm^2 to achieve the target mean molecular area of 30 $Å^2$/chain. A freshly cleaved HOPG substrate mounted on the automated dipper was brought down into contact with the air–water interface, with the substrate oriented nearly parallel to the subphase, at a rate of 2 mm/min. Contact was maintained for 4 min before withdrawing the HOPG from the interface at a rate of 2 mm/min. The substrate was then unmounted from the dipper and immediately blown dry with UHP N_2. The alkyldiynamine monolayers were polymerized under a UV lamp (λ_{max} = 254 nm, 8 W), with ~2 cm between the lamp and substrates, for the time indicated in the manuscript (0–90 min). Substrates were placed in locations under the lamp with equivalent photon flux. Photon flux was measured by a TandD TR-74U illuminance UV recorder (Matsumoto, Japan). The UV sensor was illuminated by the UV lamp used for polymerization for 20 min, and the stable photon flux was read from the instrument.

3.4.3 Preparation of PDMS stamps

Sylgard 184 silicone elastomer base and curing agent were thoroughly mixed at a 10:1 (m/m) ratio. To prepare a set of stamps, we placed a 2 cm * 5 cm metal grid with a mesh size of 50 µm * 50 µm in a petri dish and poured PDSM mixture over the grid. The mixture was then degassed under vacuum for 30 min to remove bubbles in the PDMS mixture. The PDMS was cured for 24 h at 60 ^{o}C and the metal grid was gently exfoliated from the PDMS surface. The micropatterned PDMS was then cut into 1 cm * 1 cm squares to match the size of HOPG substrates. Prior to microcontact printing, stamps were cleaned by sonication in a mixture of Milli-Q water, methanol and ethanol (v/v/v = 1/1/1) for 60 min, and placed in an oven at 60 ^{o}C for 1 h to remove polar solvent. Stamps were then immersed in hexane for 6 h, replacing the solvent every 2 h, to remove organic residues from the pores. Stamps were placed with the pattern side up in a petri dish and dried in an oven at 60 ^{o}C for at least 24 h prior to use.

3.4.4 Microcontact printing (µCP) of alkydiynamines

The process used for µCP of striped phases were adapted form reported methods, [9 46] described briefly below. A 2.5 mg/mL alkydiynamine solution was prepared in hexane/isopropanol (v/v = 3/2) solution and diluted to 0.4 mg/mL by addition of ethanol. Stamps were inked with the solution for 1 min and dried in atmosphere for 1 h at room temperature. To print striped phases on HOPG, the inked surface of a stamp was placed on a freshly cleaved HOPG, which was set on a hot plate at 50 ^{o}C for 15 min. Stamp–substrate contact was maintained for 1 min; the HOPG sample remained on the heated hot plate for a further 1 min after removal of the stamp. µCP monolayers on HOPG substrates were polymerized under UV illumination for 60 min, as described above, then covalently transferred to PDMS as described below.

3.4.5 Covalent transfer of striped phase polydiacetylene layers from HOPG to PDMS

Transfer of alkyldiynamine monolayers from HOPG to PDMS was performed using minor modifications of a protocol we developed previously for low-temperature transfer of COOH striped phases.[66] SYGARD 184 silicone base and crosslinker (curing agent) were mixed in a 10:1 (mass/mass) ratio. The mixture was stirred for 10 min to maximize homogeneity in distribution of the components, before pouring the PDMS mixture over HOPG substrates functionalized with

alkyldiynamine monolayers. The PDMS-coated substrates were placed in a vacuum chamber for 30 min to remove bubbles. Subsequently, PDMS-coated substrates were cured in an oven at 38 °C for 39 h; the relatively long curing schedule at low temperature was chosen to avoid thermal polymerization of alkyldiynamines. Exfoliation of the cured PDMS from the HOPG substrates yielded PDMS surfaces functionalized with striped phases of amines; these were stored in closed sample holders under ambient conditions prior to fluorescence characterization.

3.4.6 Synthesis of CdSe nanoparticles (NPs)

The synthetic route for CdSe NPs was adapted from previously reported methods[74, 75], described briefly here. Se (83 mg) powder was dissolved in TOP (0.62 mL) at 120 °C under vacuum. Meanwhile, a mixture of CdO (86 mg), ODPA (400 mg) and TOPO (4 290 mg) was heated to 150 °C and was vigorously stirred under vacuum for 60 min to remove O_2. Subsequently, the system was fluxed with N_2 and the temperature was raised to 300 °C, inducing formation of a Cd-complex. When the solution become colorless, another 2.6 mL TOP was injected into the hot mixture before increasing the temperature to 380 °C. Se-TOP solution was added to the Cd-complex solution through fast injection, and the heating mantle was removed immediately after the completion of the injection. The solution was cooled to 70 °C before diluting with 5 mL toluene. The as-synthesized nanoparticles were washed three times with toluene/methanol (v/v = 1/3) solution and were collected by centrifuging at 5000 rpm for 5 min. The washed nanoparticles were redispersed in 10 mL toluene and stored in dark conditions.

3.4.7 Specific adsorption of CdSe NPs on PCD-NH_2

Washed CdSe NPs were diluted 5x with cyclohexane and filtered through a 0.2-µm PTFE syringe filter to remove large aggregates. To allow adsorption CdSe on µCP squares (while preventing nonspecific deposition by sedimentation), PCD-NH_2/PDMS samples were inverted and suspended in contact with 1 mL CdSe NP solution. The surface of the sample was maintained in contact with the CdSe NP solution for 2 min, then was washed with 1 mL cyclohexane before being blown dry by N_2.

3.4.8 Functionalization of PCD-NH2 with Rhodamine Red-X (RR) succinimidyl ester

Rhodamine red (RR) succinimidyl ester was used to covalently functionalize NH_2 of sPDAs on PDMS.[9] In a typical functionalization reaction, 0.5 mg RR succinimidyl ester was dissolved in 1 mL DMF; the sPDA-functionalized PDMS substrate was suspended above the RR solution with only the patterned side contacting the solution surface. Reactions were carried out for 18 h at room temperature under N_2 atmosphere, with continuous stirring of the RR solution. Following reaction, the PDMS substrate was rinsed with 2 mL DMF and then sonicated in DMF for 2 h, replacing DMF every hour. Finally, the functionalized PDMS substrate was sonicated for 2 h in a mixture of 1:1:1:1:1 (v/v/v/v/v) methanol, ethanol, isopropanol, Milli-Q water, and DMSO, then dried at 60 °C

3.4.9 Atomic force microscopy (AFM) imaging and image analysis

A Veeco MultiMode with a Nanoscope V controller (Bruker Instruments, Billerica, MA) was used to acquire AFM images in tapping mode, with Bruker RFESP-75 tips (nominal force constant 3 N/m and radius of curvature <12 nm) in an ambient environment. AFM images were processed with Gwyddion SPM software (http://gwyddion.net). Prior to quantitative analysis, mean plane subtraction and row alignment procedures, such as fitting to median or median differences, were performed for all raw data files. Gwyddion software was also used to perform polymer counting and length measurement on 0-min and 20-min polymerized samples. For each sample, counts and measurement were collected from 3 discrete 500 nm * 500 nm locations with resolvable lamellar structures and lifted backbones.

3.4.10 Scanning electron microscopy (SEM) imaging

All scanning electron micrographs were acquired using a Teneo VolumeScope SEM (Thermo Fisher Scientific, Hillsboro, OR). Samples were mounted to standard SEM pin stub mounts with double-coated carbon conductive tape. To minimize surface charging during image acquisition, and to promote enhanced electrical contact between the sample and the specimen disk, PELCO colloidal silver was applied around the periphery of the HOPG substrate. High resolution imaging of striped phase PDA layers on HOPG was achieved using the in-column T3 (Trinity) detector in OptiPlan mode at working distances of 3.5–5.5 mm. Using a 32-µm aperture and 5.00

kV accelerating voltage, beam currents in the range of 0.4–2.0 nA produced the best resolution of the monolayers.

3.4.11 Confocal fluorescence microscopy and spectral imaging

Fluorescence images and emission spectra were acquired using a Zeiss LSM 880 Axio Examiner upright confocal microscope. Alkyldiynamine-functionalized PDMS samples were covered with 0.17-mm glass cover slip and focused through a 20x objective (plan-apochromatic, dry, NA = 0.80). For studies of polymerization kinetics, excitation was carried out using a 488-nm Ar laser at 100% power. Emitted fluorescence was detected by a 32-channel GaAsP spectral photomultiplier detector with a pinhole size set to 1 Airy unit. All fluorescence images and corresponding spectra were collected at a resolution of 2856 * 718 pixels with 8-bit depth. Unidirectional horizontal scans were averaged 16 times/line with a dwell time of 11.75 µs/pixel. Emission spectra were collected from 495–691 nm with a bin width of 8.9 nm. PDMS emission at 513 nm was subtracted from monolayer spectra to observe the fluorescence from PDA monolayers at longer wavelengths. For CdSe adsorption and RR functionalization measurements, to avoid detector saturation, alternative excitation conditions were used. In CdSe adsorption experiments, a 405-nm or 488-nm laser set to 50% power was used for excitation. A 561-nm laser was set to 10% power was used for measurements of RR post-functionalization of -NH2. For these experiments, images were collected at a resolution of 1024 * 1024 with a scan speed of 11.75 µs/pixel. Other conditions for image and spectral acquisition were maintained as described for kinetics measurements. Analysis of fluorescence timepoints

3.4.12 Wide-field fluorescence microscopy

An Olympus DP71 color camera acquired all epifluorescence images with an ISO value of 200. Images were collected with a 40x (metallographic, plan-fluorite aberration correction, NA = 0.75) bright field objective with a resolution of 1024 * 916 pixels. UV and blue wavelength excitation experiments were carried out using filter cubes with parameters below:

excitation filter	emission filter	dichromatic filter	exposure time
330-385 nm	420 nm	400 nm	0.5 s
460-490 nm	520 nm	500 nm	2 s

3.4.13 Molecular modeling

Visualization of structures and energy minimization are carried out by software packages Maestro and Macromodel (Schrödinger, Cambridge, MA). Energy minimization was achieved by using OPLS3e force field in vacuum with extended cutoffs van der Waals, electrostatic and hydrogen bonding interactions. The Polak-Ribiere conjugate gradient (PRCG) algorithm was selected to approach minimum energies with 10, 000 maximum runs and 0.005 kJ/mol-Å convergence threshold for the RMS gradient of the energy with respect to the coordinates. Diynamine monolayer models on HOPG were composed of 4 rows of 16 molecules each, with rows of paired headgroups in the center.

3.4.14 Image analysis.

AFM and SEM images were processed with Gwyddion SPM software (http://gwyddion.net). Prior to quantitative analysis, mean plane subtraction and row alignment procedures, such as fitting to median or median differences, were performed for all raw data files. Gwyddion software was also used to perform polymer counting and length measurement on 0-min and 20-min polymerized samples. For each sample, counts and measurement were collected from 3 discrete 500 nm * 500 nm locations with resolvable lamellar structures and lifted backbones.

3.4.15 Measurement of degree of polymerization.

In Figure 3.4 and 3.7, to assess differences in diacetylene polymerization based on monomer structure, we calculated both number-average and weight-average degrees of polymerization (DP_n and DP_w). In bulk polymer experiments, these values would typically be calculated from the number-average and weight-average molecular weights (M_n and M_w, respectively), using the following equations:

$$DP_n = \frac{M_n}{M_0}$$

$$DP_w = \frac{M_w}{M_0}$$

where M_0 represents the molecular mass of the diacetylene monomers.

Because the AFM measurement strategy measures polymer lengths rather than polymer mass, the DP of each polymer is recorded directly using the formula given on the previous page, and these

values are used to calculate DP_n and DP_w as follows, where N_i is the number of polymers with degree of polymerization DP_i:

$$DP_n = \frac{\sum_i N_i DP_i}{\sum_i N_i}$$

$$DP_w = \frac{\sum_i N_i (DP_i)^2}{\sum_i N_i DP_i}$$

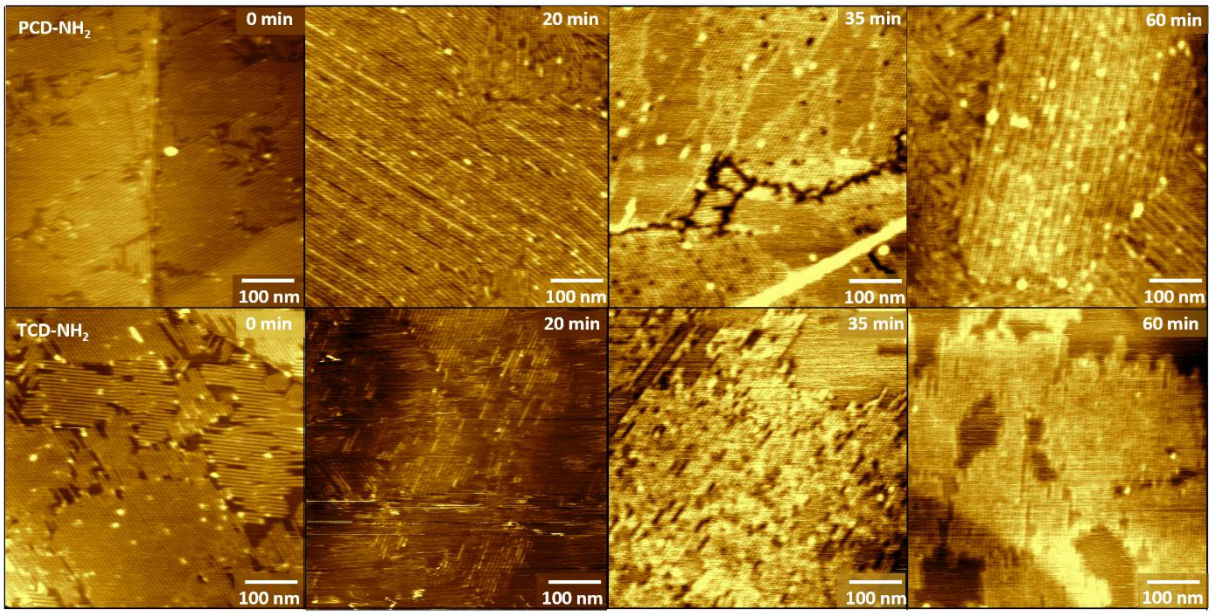

Figure 3.7 AFM images of alkyldiynamine monolayers (PCD-NH_2, top, and TCD-NH_2, bottom) on HOPG, with polymerization times specified on each image.

3.4.16 Calculation of PDMS transfer probabilities of polymers

We observed that TCD-NH_2 monolayers produce lower fluorescence emission than PCD-NH_2 monolayers, even when both monolayers appear to reach essentially full conversion to polymer by AFM. A similar phenomenon had been observed for PCD-COOH monolayers in comparison with TCD-COOH monolayers. Because both TCD-NH_2 and PCD-COOH also produce *shorter* polymers, as measured by AFM, we decided to evaluate whether this might result from lower probabilities of transfer for shorter polymers.

Therefore, we used simple probabilistic models to evaluate the likelihood of transfer of PDAs based on polydiacetylene length. The goal was to establish the expected number of PDA units that transfers to PDMS for a population of polymers with a certain distribution of lengths.

The number of PDA units transferred should, to a first approximation, be proportional to the fluorescence emission intensity measured experimentally.

As inputs, we used polymer lengths for hundreds of individual PDAs measured from AFM images, for both PCD-NH_2 and TCD-NH_2; we also used this method to evaluate populations of polymer lengths for PCD-COOH and TCD-COOH collected for a previous study.

The model presumes that the transfer probability for an individual polymer depends on the number of repeat units in the polymer (N); polymer length is measured from AFM images, based on the lengths of the lifted PDA backbones. These initial length measurements are tabulated in Fig. 3.8-9. Polymer length in nm is then divided by the width of an individual repeat unit (0.45 nm) in a striped PDA molecular row to yield N:

$$N = \frac{polymer\ length}{0.45\ nm}$$

We approximate that each repeat unit in the PDA represents one possible site for crosslinking to the PDMS network via reaction with a Si-H bond in the crosslinker. The exact probability of crosslinking is not known, but is presumed to be relatively low, since the mesh size of the PDMS network is ~10 nm, meaning that perhaps 1 site in 20 along the PDA chain is positioned to connect to the network. We tested a range of probabilities ($p = 0.005–0.05$) to represent 1 in 20 sites to 1 in 200 sites crosslinking.

We also calculated probabilities with a range of assumptions regarding the minimum *number* of total crosslinks to the PDMS network ($n = 1–4$) required to exfoliate a PDA. We note that it is possible that the number of crosslinks required to transfer a PDA may increase with PDA length, but assuming n to be constant provided a convenient approximation for initial calculations. For each polymer, we calculated the probability of transfer for each set of assumptions described above:

$$P_n(N) = C(N,n) \times p^n \times (1-p)^{N-n}$$

Although each PDA either transfers or does not, fluorescence intensity measurements are made based on very large numbers of polymers, so we calculated an expected value (N_{exp}) for number of repeat units transferred, for each polymer in our AFM population. This value represents average PDA repeat units transferred to PDMS from polymers of this length, assuming that this polymer is representative of many transfer events, so that averaging is possible:

$$N_{exp} = N \times P_n$$

Expected values were summed for all the polymers in each AFM population, for each probability and crosslinking condition pair (p and n). This created an expected value for the total number of PDA units transferred for each molecule, under each choice of per-unit reaction probability, and the number of reactions required for transfer. Values of N_{exp} were summed across the entire population for each n, p condition pair, to generate an estimate of the relative amount of PDA transfer over a larger area.

Each graph in Figure 5 in the main manuscript uses sets of values calculated in this way, and in some cases makes comparisons with known ratios of fluorescence emission for pairs of molecule types. That is, because we know that the emission intensity from fully-polymerized TCD-NH_2 is ~0.6 x the emission from fully-polymerized PCD-NH_2, we can use that to help constrain the range of p and n that would produce the observed difference in emission.

Polymer length (nm) – TCD-NH_2														
103.2	137.3	11.7	47.7	140.4	41.4	54.9	66.0	140.0	108.3	56.6	195.1	194.5	88.0	213.2
64.5	241.5	294.9	453.3	62.1	53.5	35.9	19.7	29.7	12.1	115.0	92.6	35.9	45.9	27.3
6.2	4.2	12.2	3.1	6.1	5.5	2.8	4.1	5.3	7.0	5.0	4.5	3.7	4.2	3.9
38.7	193.5	51.8	50.3	16.8	146.6	35.6	84.5	50.0	18.4	29.5	93.7	23.6	25.2	27.4
54.8	18.0	15.1	18.0	37.4	34.4	22.5	10.2	40.9	9.3	62.7	58.5	55.7	53.8	53.4
35.0	20.8	46.6	53.3	21.8	35.6	25.5	29.7	25.0	24.4	47.8	26.3	55.1	37.4	26.7
49.6	27.5	78.5	32.4	48.3	46.0	46.3	15.9	40.4	67.3	82.3	40.1	33.8	30.1	75.3
53.4	97.4	86.5	21.9	15.6	38.7	23.0	36.0	94.1	59.6	68.8	94.0	60.2	35.2	34.3
39.9	20.2	19.9	57.1	65.1	44.6	29.3	46.4	29.9	41.4	49.2	51.1	58.5	171.3	166.9
34.0	35.2	35.9	26.7	23.3	31.5	49.8	58.7	55.9	63.6	80.2	65.6	72.5	72.6	65.6
47.7	42.4	49.4	55.9	47.4	50.0	43.7	50.8	53.3	69.4	61.9	59.0	29.4	29.7	28.8
93.1	38.2	38.1	51.0	46.3	116.4	79.3	57.5	24.5	34.3	52.1	15.7	35.4	33.6	42.7
36.8	7.9	9.8	8.0	32.8	26.6	23.1	22.4	31.4	45.5	18.9	5.3	16.5	17.7	34.0
20.7	57.8	15.0	9.5	18.8	15.7	8.2	34.2	26.3	4.6	4.8	7.7	18.9	2.1	2.7
8.2	19.5	47.1	45.1	21.0	15.6	20.4	15.6	20.1	13.9	13.0	43.1	15.3	47.8	36.6
24.3	19.3	43.1	10.5	33.4	36.3	9.0	15.8	11.4	8.1	38.1	22.3	28.2	28.2	60.1
9.2	40.1	8.7	29.0	13.3	3.1	36.3	53.4	55.5	25.0	30.9	71.3	32.6	5.9	53.6
46.4	25.0	33.3	20.5	36.3	12.7	15.3	64.5	80.0	56.9	30.1	25.5	30.4	20.9	65.8
83.7	28.2	74.5	217.8	54.3	26.0	29.5	72.1	70.7	61.5	60.7	38.5	23.8	89.3	88.8
61.8	72.1	73.0	153.7	23.0	9.0	21.1	41.5	35.0	107.4	80.4	27.6	181.1	39.4	28.5
22.5	44.9	3.1	9.8	57.6	42.0	57.1	17.8	8.3	21.7	28.5	19.6	25.7	12.1	52.0
12.2	53.8	101.6	104.9	52.5	38.2	27.8	123.1	64.5	25.6	80.7	27.6	40.1	50.1	56.9
31.3	31.5	80.1	39.0	53.4	50.3	73.5	34.6	56.0	97.1	36.2	80.8	42.2	23.9	33.6
12.7	61.5	112.9	35.2	43.0	29.7	66.8	23.5	36.3	42.3	77.2	51.8	9.0	30.3	41.1
46.0	40.8	39.2	19.6	46.9	32.5	21.7	25.4	16.6	23.6	14.8	33.2	10.7	47.7	56.4
42.7	74.0	66.7	61.0	46.6	46.3	116.4	79.3	57.5	24.5	34.3	52.1	15.7	35.4	33.6
259.7	159.8	209.8	32.1	103.3	264.3	39.0	122.8	71.8	166.7	202.9	167.7	125.9	94.2	80.1
26.6	46.9	76.9	70.8	37.3	64.6	87.4	59.8	15.9	3.9	6.2	4.5	4.5	3.8	7.3
4.2	3.0	2.0	5.6	3.1	4.2	4.5	3.4	3.3	14.8	10.2	2.6	9.1	127.1	43.5
27.5	13.3	87.2	71.3	67.1	55.1	24.6	83.8	86.7	18.4	14.9	11.0	46.3	45.8	58.2
29.6	23.5	91.0	92.7	27.4	107.1	104.9	123.3	20.2	116.4	114.7	32.8	24.1	30.9	58.7
35.1	68.8	49.7	36.9	46.3	56.2	31.8	21.1	34.9	49.8	25.5	35.3	19.9	54.6	27.1
48.5	33.1	72.9	70.9	134.1	46.0	49.1	30.9	41.6	12.0	13.1	59.5	64.9	50.4	50.6
119.5	195.3	44.6	37.0	53.2	16.1	38.4	12.8	23.0	62.0	19.7	52.1	70.1	46.8	55.6
39.5	69.9	30.1	29.9	34.4	48.7	56.6	61.9	152.7	69.3	65.4	128.5	93.7	105.2	54.6
63.6	58.0	82.0	90.7	68.2	69.6	75.8	77.7	66.1	79.1	74.9	18.9	23.9	31.8	37.4
117.8	111.5	117.7	42.5	25.9	242.6	67.3	78.5	103.9	161.2	149.5	48.5	47.7	56.4	60.0
74.0	66.7	61.0	46.6	61.7	53.8	21.8	24.5	20.1	66.4	41.2	26.9	45.5	21.4	19.8
26.6	19.6	15.7	10.3	10.0	14.5	10.4	10.4	16.1	46.1	18.1	15.9	20.1	19.2	17.9
15.0	5.3	20.0	15.7	11.3	36.4	25.0	14.7	18.6	13.9	32.0	43.1	25.7	17.4	18.9
55.0	7.5	13.1	7.1	55.8	70.5	14.4	10.1	6.5	5.3	11.5	14.7	17.2	16.8	8.8
5.7	11.4	36.6	31.7	13.6	24.9	25.5	10.9	11.0	24.4	18.8	10.1	17.4	13.1	69.1
27.1	98.3	58.2	68.0	6.3	5.0	9.0	9.6	6.2	30.3	21.1	22.5	120.3	21.9	34.8
29.3	41.7	41.4	60.0	71.2	63.4	231.5	22.5	15.4	53.4	85.9	20.3	26.6	80.8	20.6
181.1	24.5	55.9	27.4	29.8	37.4	23.0	56.0	25.0	95.2	72.5	7.9	62.1	34.9	221.6
34.2	18.6	52.2	29.6	16.7	41.6	23.5	68.3	29.0	54.7	25.4	28.6	23.5	51.8	54.7
46.1	71.5	23.3	37.9	37.5	65.0	26.7	31.7	38.8	49.0	8.4	16.7	91.7	23.2	24.6
173.0	42.4	42.4	36.8	14.9	13.3	73.7	58.0	23.3	12.4	130.2	13.6	102.3	36.7	37.1
29.4	37.1	10.0	9.8	14.7	7.8	23.5	68.5	45.9	8.1	24.7	34.2	39.1	45.2	39.4
19.6	23.5	26.5	12.7	43.0	16.6	23.5	12.7	28.3	14.7	14.7	51.0	30.6	18.6	24.5
60.0	93.1	38.2	38.1	51.0										

Figure 3.8 Polymer lengths of TCD-NH_2 at early polymerization timepoints from the measurement of linear protrusions in AFM images.

Polymer length (nm) – PCD-NH_2														
17.9	12.6	11.1	9.9	12.0	6.8	13.5	19.1	13.0	14.2	23.7	37.2	15.4	9.2	9.6
8.2	10.0	19.2	17.9	11.3	43.5	10.5	13.4	23.9	63.9	21.0	19.4	23.5	19.8	28.4
10.5	15.9	12.3	9.0	14.0	16.7	11.4	14.1	10.1	86.9	124.5	59.6	25.8	25.4	138.8
119.4	102.5	99.1	117.4	165.3	101.1	43.7	168.3	184.2	86.6	123.2	94.8	56.2	76.6	77.0
93.5	47.8	93.5	48.6	90.5	88.5	73.0	130.3	153.5	98.0	79.4	49.1	70.3	46.0	90.8
182.5	114.5	61.1	69.8	69.4	49.3	33.2	87.5	44.6	168.1	141.3	138.9	123.4	112.0	115.8
84.5	68.3	64.8	171.1	91.8	156.5	195.6	73.4	100.8	177.9	55.8	73.6	42.1	237.4	100.2
13.7	13.0	11.3	9.3	17.2	12.0	24.0	32.5	25.9	23.9	19.2	60.8	23.7	23.4	10.8
29.7	8.8	7.3	19.5	13.3	24.7	29.3	21.5	42.7	20.1	23.5	26.8	22.4	6.8	11.7
15.7	12.7	10.8	9.8	7.8	13.6	10.7	12.7	22.0	22.2	11.7	7.8	22.0	13.3	17.1
13.8	10.4	11.9	41.6	15.8	15.2	16.6	16.5	8.9	17.6	13.2	9.9	9.9	8.2	9.6
26.0	18.6	22.6	30.3	12.4	11.0	9.3	10.2	10.3	14.2	8.5	25.2	9.4	6.8	18.9
14.2	17.6	17.6	13.2	4.4	11.3	16.6	6.0	20.0	25.4	32.4	12.4	21.7	24.1	16.1
46.2	361.7	293.7	197.6	69.2	89.9	149.8	142.5	143.0	185.7	165.2	161.2	147.3	189.0	78.7
186.5	183.1	139.8	225.5	100.0	80.7	151.6	277.2	149.1	153.0	268.7	205.2	90.8	45.9	198.9
101.9	66.1	91.1	116.2	151.5	90.7	116.9	162.0	75.2	111.5	143.1	271.4	197.1	219.2	191.5
91.4	179.8	81.3	42.5	78.6	141.5	128.2	74.8	90.7	128.9	78.2	50.8	113.9	74.2	101.9
115.9	125.4	117.4	49.5	81.6	178.4	173.6	105.2	87.3	52.8	74.1	126.1	134.0	157.0	121.4
119.4	111.2	67.7	61.5	18.8	20.1	23.4	59.4	46.9	189.8	236.8	429.7	408.7	233.7	123.1
134.9	129.8	129.9	79.0	32.8	31.4	28.6	42.8	22.0	23.1	58.5	59.9	30.3	62.6	61.0
112.0	69.0	94.7	92.5	74.0	72.8	62.2	78.6	64.7	73.0	64.9	16.2	23.9	24.7	32.4
41.9	275.5	246.5	203.1	168.9	178.7	28.1	51.5	151.2	93.4	156.7	250.9	19.0	16.4	33.6
8.5	12.7	13.6	49.5	82.7	49.5	173.3	221.4	206.3	196.4	174.7	35.0	14.2	16.7	26.3
113.9	121.9	180.3	113.7	42.7	35.3	35.5	96.9	40.7	28.2	32.3	68.5	76.5	38.1	46.3
40.3	44.0	132.7	134.7	129.1	153.9	166.5	76.1	88.4	17.9	10.9	22.5	8.5	29.5	35.5
9.2	31.7	25.3	28.6	28.3	35.4	28.3	13.9	20.3	13.0	6.5	7.1	6.1	8.5	18.1
10.0	10.1	11.8	12.8	13.7	12.0	18.2	23.0	7.3	18.0	10.0	22.2	12.4	25.3	11.6
116.7	126.1	73.9	116.7	94.8	40.6	159.4	156.9	116.7	126.3	102.4	69.9	87.8	103.4	74.8
31.2	79.0	99.7	72.6	50.2	54.6	61.2	114.5	131.1	98.2	95.7	98.6	54.7	67.3	51.5
94.2	67.9	103.4	89.5	72.3	45.9	95.2	92.9	127.8	64.3	62.4	66.0	75.5	97.0	104.3
99.3	63.6	94.8	55.0	223.4	61.5	220.1	127.4	157.3	121.6	108.4	112.3	177.1	174.5	202.9
60.6	88.4	55.8	21.7	33.9	15.6	42.7	26.7	11.1	10.6	10.7	18.1	14.0	44.4	28.0
24.0	29.3	13.7	16.7	15.6	15.1	22.9	8.3	8.8	14.1	11.7	12.7	18.5	33.7	13.7
19.4	22.3	17.1	20.4	21.4	11.7	7.8	14.2	13.2	14.7	14.6	9.4	5.9	18.7	12.4
15.7	8.4	11.0	14.8	20.4	9.6	7.3	7.3	14.6	11.4	8.8	24.4	8.5	12.2	12.2
9.8	8.8	11.9	7.4	8.3	14.8	7.0	14.8	6.4	6.4	5.4	16.7	15.7	4.9	10.4
10.3	23.2	32.7	16.3	16.1	9.5	12.3	15.1	19.0	20.7	12.2	11.0	33.4	15.6	11.3
15.1	13.7	12.8	8.4	16.1	23.2	11.7	11.2	14.2	8.8	9.3	16.1	13.4	125.0	181.4
206.1	323.7	244.6	169.6	174.3	276.2	187.0	110.1	125.4	161.1	83.3	81.5	154.6	197.5	128.4
86.9	81.9	314.2	116.1	128.8	171.6	56.8	235.5	103.5	175.6	146.3	172.7	200.6	183.7	120.0
152.6	136.4	283.3	93.1	110.1	97.2	115.8	65.0	72.7	57.9	26.0	91.4	126.8	117.1	94.3
88.3	106.3	72.1	114.6	77.0	224.1	60.5	78.0	106.4	62.0	45.7	137.4	162.0	136.9	37.2
118.0	26.6	41.5	31.7	29.4	144.4	122.4	63.0	68.5	42.1	73.6	84.9	41.3	86.0	115.4
194.5	121.3	234.3	116.8	262.8	316.3	176.7	170.2	143.3	81.8	135.3	126.5	86.2	84.9	63.8
23.4	32.6	83.6	66.1	61.4	60.9	56.6	66.7	58.0	61.2	31.8	100.1	104.0	95.5	112.0
29.2	34.6	36.0	35.8	42.1	42.8	66.8	63.9	161.0	170.8	201.8	198.8	12.7	12.7	20.1
109.5	240.7	55.0	24.2	56.4	47.6	13.1	18.0	67.6	30.4	27.1	21.7	46.7	10.3	14.0
156.2	190.9	193.8	186.8	116.7	64.5	149.7	46.9	53.8	61.7	72.1	75.9	39.8	59.3	92.6
50.0	40.0	82.1	78.1	76.7	47.4	34.1	37.5	33.2	24.1	22.5	31.8	28.9	33.0	40.7
37.3	44.0	9.0	10.1	170.9	16.5									

Figure 3.9 Polymer lengths of PCD-NH_2 at early polymerization timepoints from the measurement of linear protrusions in AFM images.

3.4.17 Analysis of fluorescence images.

Fluorescence images for timepoint studies were analyzed and converted to .bmp format via Zeiss Zen software (Blue version) (Carl Zeiss NTS Ltd., Jena, Germany). Fluorescence intensities

of transferred TCD-NH_2 and PCD-NH_2 monolayers were acquired from 3–6 samples at each of the following polymerization timepoints:

0 min, 20 min, 35 min, 40 min, 60 min, 90 min.

Three regions of interest (ROI) were selected in the in-focus area of each sample to calculate means and standard deviations for emission intensities. If samples included focused regions with obvious differences in brightness, we performed ROI analyses on areas with varying brightness to capture sample variability.

For fluorescence data at each timepoint, the quartile method was used to identify outliers and establish error bars. To filter outliers, upper and lower boundaries for included data points are determined from the interquartile range (IQR). IQR is defined by the difference between the 25th (Q1) percentile and 75th percentile (Q3) of the data values, which is calculated as Q3–Q1. Upper and lower bounds of the data set are calculated as follows: upper bound = Q3 + 1.5*IQR, lower bound = Q1 – 1.5*IQR. The mean values are calculated excluding points outside the boundaries, if present.

In Chapter 3.2, we graphed emission intensity of TCD-NH_2 and PCD-NH_2 monolayers transferred to PDMS with specified polymerization times on HOPG, ranging from 0–90 min. Each data point results from the mean of 25–30 regions from 5–6 samples. In Figures 3.10-13, we tabulate the fluorescence intensities (with standard deviations) from each measured region of interest (ROI).

0 min mean	0 min stdev	20 min mean	20 min stdev	35 min mean	35 min stdev	40 min mean	40 min stdev	60 min mean	60 min stdev	90 min mean	90 min stdev
1.66	0.69	2.93	1.19	5.84	2.20	11.25	3.18	9.67	2.74	9.62	3.48
2.07	0.64	2.21	0.66	4.51	1.55	9.09	2.71	8.06	2.30	9.09	3.81
1.32	0.53	1.66	0.71	4.31	1.78	9.89	3.35	9.18	2.89	9.94	3.86
1.90	0.46	2.86	1.17	5.11	3.31	3.50	1.75	6.50	2.35	7.78	3.98
2.74	0.92	3.93	1.51	4.51	1.55	3.98	1.86	4.95	1.73	5.78	3.32
2.42	0.69	3.90	1.31	3.52	1.51	5.20	2.92	5.91	2.14	6.50	1.99
1.73	0.76	2.04	0.29	4.21	1.89	5.35	1.81	13.97	3.74	6.76	2.50
2.59	0.98	2.04	0.39	2.56	0.76	5.80	1.72	15.84	4.36	5.46	1.69
2.42	0.73	2.01	0.45	7.03	3.05	4.81	1.90	14.71	3.03	4.99	1.93
1.19	0.17	1.16	0.37	9.45	3.82	6.07	1.75	7.30	2.01	9.58	2.39
1.98	0.39	1.27	0.47	7.80	2.36	4.72	3.24	14.52	4.78	9.61	2.33
1.05	0.21	1.77	0.74	5.17	1.69	5.15	1.79	7.30	2.01	9.16	2.17
2.22	1.27	2.66	1.16	5.34	1.96	4.18	2.03	8.69	1.94	2.56	0.76
0.88	0.86	3.21	1.24	5.63	2.15	4.35	1.92	8.40	2.37	3.30	1.42
0.83	0.82	3.26	1.19	4.59	1.49	8.48	2.77	4.69	1.50	3.53	1.62
2.45	1.31	2.93	1.19	6.73	2.02	3.35	1.24	6.41	2.18	7.87	4.19
2.59	1.52	3.93	1.51	6.43	2.23	6.15	2.31	6.64	2.07	7.39	4.43
2.43	1.38	3.90	1.31	7.56	1.96	7.27	2.47	11.44	4.12	6.56	2.92
3.54	1.74	1.27	0.47	6.21	1.96	4.26	2.02	6.09	2.12	6.14	2.43
1.96	1.20	1.27	0.46	5.50	1.53	5.14	1.72	8.27	2.13	8.28	3.08
1.72	1.12	1.98	0.25	13.05	4.98	4.66	1.63	6.86	1.88	10.15	3.61
2.49	1.36	3.82	1.24	12.45	2.99	4.85	2.01	7.80	2.68	7.26	8.59
2.39	1.40	4.46	1.39	9.81	3.33	4.88	2.28	7.51	2.17	6.44	2.09
2.64	1.57	5.61	1.61	9.79	2.57	3.77	1.22	4.95	1.73	7.53	2.81
1.53	1.18	3.82	1.24	3.92	1.31	4.08	1.36	6.86	2.77	7.64	3.11
1.87	1.34	3.90	1.30	2.98	0.99	1.56	1.31	10.10	2.64	14.60	3.69
1.88	1.41			5.06	1.42	4.80	1.97	5.32	1.52	9.04	3.25
				4.74	1.92	7.94	2.25	7.04	1.84	11.95	3.06
				4.61	1.39	7.02	1.88	6.96	2.11	10.22	2.52
				4.26	1.57	5.70	1.69	13.33	5.02	11.86	3.23
				3.87	2.10	4.22	1.40				
				4.12	1.42						

Figure 3.10 Mean and standard deviation fluorescence values for regions of interest collected on TCD-NH_2/PDMS samples at the indicated polymerization timepoints.

	0 min	20 min	35 min	40 min	60 min	90 min
int	**2.09**	**2.82**	**5.44**	**5.05**	**7.63**	**7.89**
std	0.63	1.33	1.88	1.42	2.29	2.33
int/std	0.30	0.47	0.35	0.28	0.30	0.29
Q1	**1.68**	**1.99**	**4.41**	**4.24**	**6.54**	**6.45**
Q3	**2.45**	**3.88**	**7.03**	**6.11**	**9.54**	**9.60**
IQR	0.77	1.89	2.62	1.87	3.01	3.15
lower bound	0.52	-0.84	0.49	1.44	2.03	1.72
upper bound	3.60	6.71	10.96	8.92	14.05	14.33

Figure 3.11 . Statistical analysis of fluorescence emission from TCD-NH_2/PDMS regions of interest analyzed at each timepoint.

0 min mean	0 min stdev	20 min mean	20 min stdev	35 min mean	35 min stdev	40 min mean	40 min stdev	60 min mean	60 min stdev	90 min mean	90 min stdev
1.50	0.70	5.76	2.20	3.79	1.49	13.93	5.55	14.89	5.65	12.66	3.68
1.78	1.00	4.47	1.93	3.84	1.27	10.53	3.82	18.27	3.55	11.81	3.60
1.60	0.76	3.17	1.28	3.46	1.21	16.00	4.94	13.09	3.94	10.30	3.05
2.15	0.96	4.73	2.27	10.03	3.06	17.00	6.18	7.16	2.16	17.44	3.83
2.21	1.00	3.36	1.74	8.30	3.03	11.52	3.52	11.21	2.81	12.82	2.87
2.24	1.09	5.89	2.97	10.08	2.88	14.98	3.21	11.21	2.81	13.16	3.78
1.34	0.64	7.20	2.17	8.23	2.81	10.62	4.93	16.08	3.66	17.93	3.65
1.21	0.51	4.08	1.38	6.95	2.27	10.96	2.77	15.06	3.43	16.08	3.66
1.33	0.61	9.03	2.71	10.15	3.43	10.60	3.01	13.00	2.87	16.14	3.62
0.41	0.57	7.48	2.11	9.29	2.59	5.62	1.68	6.46	2.23	6.30	1.86
0.82	0.77	4.77	1.49	13.15	3.68	6.95	2.12	7.05	1.94	15.01	3.36
0.88	0.75	6.85	2.59	4.51	1.35	6.79	1.95	11.67	3.20	13.05	3.05
1.46	1.14	3.57	1.67	8.48	2.51	5.47	1.47	10.62	3.81	15.83	3.83
1.14	0.83	2.71	1.11	4.81	1.81	6.32	1.96	5.49	1.72	12.31	2.51
1.83	0.85	3.92	1.54	8.91	3.42	6.68	1.87	20.12	4.76	9.94	2.39
1.86	1.38	3.19	1.32	7.95	2.62	5.02	1.48	16.39	5.30	16.29	4.82
1.93	1.10	6.68	1.70	6.69	2.64	4.56	1.41	14.24	4.26	8.69	2.46
1.93	1.03	4.81	1.65	12.22	3.63	5.55	1.82	11.56	3.43	12.31	2.51
0.31	0.54	4.84	1.50	8.27	2.33	9.02	2.31	11.03	2.77	13.09	3.94
0.31	0.55	5.07	2.24	7.69	2.13	14.76	3.04	11.68	3.41	9.32	4.26
0.42	0.63	3.12	1.40	4.45	1.64	15.61	3.56	8.12	2.64	8.55	2.20
2.96	1.56	3.14	1.15	4.81	1.81	10.08	2.70	7.54	2.11	9.06	2.19
2.00	1.31	5.10	1.69	6.01	1.92	10.09	2.80	8.54	2.88	9.78	6.01
4.15	2.14	3.92	1.55	5.91	2.27	10.73	3.12	9.91	4.22	12.47	4.85
2.26	1.60	5.71	1.54	5.50	1.64	10.10	2.73	9.37	3.59	17.44	3.83
1.65	1.22	6.11	1.87	6.11	2.02	11.58	4.15	17.00	6.18	10.30	3.05
1.99	1.37	6.86	1.61	5.52	2.29	12.57	4.25	14.89	5.65	14.37	4.24
1.34	1.00			6.73	1.94	12.55	3.45			12.66	3.68
1.44	0.98					14.48	2.77			8.75	2.43
0.95	0.90					12.78	2.70			6.49	3.36
						14.11	2.85			8.75	2.43
										10.64	9.29

Figure 3.12 Mean and standard deviation fluorescence values for regions of interest collected on PCD-NH_2/PDMS samples at the indicated polymerization timepoints.

	0 min	20 min	35 min	40 min	60 min	90 min
int	**1.54**	**4.85**	**7.02**	**10.71**	**12.03**	**11.98**
std	0.56	1.58	2.48	3.56	3.77	3.28
int/std	0.36	0.33	0.35	0.33	0.31	0.27
Q1	**1.17**	**3.74**	**5.33**	**6.87**	**8.96**	**9.43**
Q3	**1.90**	**6.00**	**8.59**	**13.36**	**14.89**	**14.71**
IQR	0.72	2.26	3.26	6.49	5.93	5.28
lower bound	0.09	0.35	0.43	-2.87	0.06	1.51
upper bound	2.98	9.39	13.49	23.09	23.78	22.63

Figure 3.13 . Statistical analysis of fluorescence emission from PCD-NH_2/PDMS regions of interest analyzed at each timepoint.

REFERENCES

(1) Barredo, D.; Lienhard, V.; de Léséleuc, S.; Lahaye, T.; Browaeys, A. Synthetic three-dimensional atomic structures assembled atom by atom. *Nature (London)* **2018**, *561* (7721), 79-82. DOI: 10.1038/s41586-018-0450-2.

(2) Ostroverkhova, O. Organic Optoelectronic Materials: Mechanisms and Applications. *Chemical reviews* **2016**, *116* (22), 13279-13412. DOI: 10.1021/acs.chemrev.6b00127.

(3) Hubbell, J. A.; Lutolf, M. P. Synthetic biomaterials as instructive extracellular microenvironments for morphogenesis in tissue engineering. *Nature biotechnology* **2005**, *23* (1), 47-55. DOI: 10.1038/nbt1055.

(4) Kyburz, K. A.; Anseth, K. S. Synthetic mimics of the extracellular matrix: how simple is complex enough? *Annals of biomedical engineering* **2015**, *43* (3), 489-500. DOI: 10.1007/s10439-015-1297-4.

(5) Ojemyr, L. N.; Lee, H. J.; Gennis, R. B.; Brzezinski, P. Functional interactions between membrane-bound transporters and membranes. *Proceedings of the National Academy of Sciences - PNAS* **2010**, *107* (36), 15763-15767. DOI: 10.1073/pnas.1006109107.

(6) Serowy, S.; Saparov, S. M.; Antonenko, Y. N.; Kozlovsky, W.; Hagen, V.; Pohl, P. Structural Proton Diffusion along Lipid Bilayers. *Biophysical journal* **2003**, *84* (2), 1031-1037. DOI: 10.1016/S0006-3495(03)74919-4.

(7) Bang, J. J.; Rupp, K. K.; Russell, S. R.; Choong, S. W.; Claridge, S. A. Sitting Phases of Polymerizable Amphiphiles for Controlled Functionalization of Layered Materials. *J. Am. Chem. Soc* **2016**, *138* (13), 4448-4457. DOI: 10.1021/jacs.5b13179.

(8) Claridge, S. A. Standing, lying, and sitting: translating building principles of the cell membrane to synthetic 2D material interfaces. *Chemical communications (Cambridge, England)* **2018**, *54* (5), 6681-6691. DOI: 10.1039/c8cc02596g.

(9) Davis, T. C.; Bechtold, J. O.; Shi, A.; Lang, E. N.; Singh, A.; Claridge, S. A. One Nanometer Wide Functional Patterns with a Sub-10 Nanometer Pitch Transferred to an Amorphous Elastomeric Material. *ACS nano* **2021**, *15* (1), 1426-1435. DOI: 10.1021/acsnano.0c08741.

(10) Garcia, R.; Martinez, R. V.; Martinez, J. Nano-chemistry and scanning probe nanolithographies. *Chemical Society reviews* **2006**, *35* (1), 29-38. DOI: 10.1039/B501599P.

(11) Zhao, X. M.; Xia, Y.; Whitesides, G. M. Soft lithographic methods for nano-fabrication. *Journal of materials chemistry* **1997**, *7* (7), 1069-1074. DOI: 10.1039/a700145b.

(12) Giancarlo, L.; Cyr, D.; Muyskens, K.; Flynn, G. W. Scanning tunneling microscopy of molecular adsorbates at the liquid-solid interface: Functional group variations in image contrast. *Langmuir* **1998**, *14* (6), 1465-1471.

(13) Hla, S. W.; Bartels, L.; Meyer, G.; Rieder, K. H. Inducing all steps of a chemical reaction with the scanning tunneling microscope tip: towards single molecule engineering. *Physical review letters* **2000**, *85* (13), 2777-2780. DOI: 10.1103/PhysRevLett.85.2777.

(14) De Feyter, S.; De Schryver, F. C. Self-assembly at the liquid/solid interface: STM reveals. *Journal of Physical Chemistry B* **2005**, *109* (10), 4290-4302. DOI: 10.1021/jp045298k.

(15) Okawa, Y.; Takajo, D.; Tsukamoto, S.; Hasegawa, T.; Aono, M. Atomic force microscopy and theoretical investigation of the lifted-upconformation of polydiacetylene on a graphite substrate. Soft Matter, 2008; Vol. 4, pp 1041-1047.

(16) Verveniotis, E.; Okawa, Y.; Watanabe, K.; Taniguchi, T.; Taniguchi, T.; Osada, M.; Joachim, C.; Aono, M. Self-Sensitization and Photo-Polymerization of Diacetylene Molecules Self-Assembled on a Hexagonal-Boron Nitride Nanosheet. *Polymers (Basel)* **2018**, *10* (2), 206. DOI: 10.3390/polym10020206.

(17) Giridharagopal, R.; Kelly, K. F. STM-Induced Desorption of Polydiacetylene Nanowires and Reordering via Molecular Cascades. *J. Phys. Chem. C* **2007**, *111* (17), 6161-6166. DOI: 10.1021/jp070998l.

(18) Porter, A. G.; Ouyang, T.; Hayes, T. R.; Biechele-Speziale, J.; Russell, S. R.; Claridge, S. A. 1-nm-Wide Hydrated Dipole Arrays Regulate AuNW Assembly on Striped Monolayers in Nonpolar Solvent. *Chem* **2019**, *5*, 2264-2275.

(19) Lang, E. N.; Porter, A. G.; Ouyang, T.; Shi, A.; Hayes, T. R.; Davis, T. C.; Claridge, S. A. Oleylamine Impurities Regulate Temperature-Dependent Hierarchical Assembly of Ultranarrow Gold Nanowires on Biotemplated Interfaces. *ACS nano* **2021**, *15* (6), 10275-10285. DOI: 10.1021/acsnano.1c02414.

(20) Wegner, G. Topochemical polymerization of monomers with conjugated triple bonds. *Die Makromolekulare Chemie* **1972**, *154* (1), 35-48. DOI: 10.1002/macp.1972.021540103.

(21) Bassler, H. Photopolymerization of diacetylenes. In *Polydiacetylenes. Advances in Polymer Science*, Cantow, H. J., Ed.; Springer: Heidelberg, 1984; Vol. 63.

(22) Guo, C.; Xue, J. D.; Cheng, L. X.; Liu, R. C.; Kang, S. Z.; Zeng, Q. D.; Li, M. Two-dimensional self-assembly of diacetylenic acid derivatives and their light-induced polymerization on HOPG surfaces. *Phys Chem Chem Phys* **2017**, *19* (24), 16213-16218. DOI: 10.1039/c7cp02337e.

(23) Bubeck, C.; Tieke, B.; Wegner, G. Selfsensitization of the Photopolymerization of Diacetylenes Studied in Multilayers. *Berichte der Bunsengesellschaft für Physikalische Chemie* **1982**, *86* (6), 495-498. DOI: 10.1002/bbpc.19820860604.

(24) Okawa, Y.; Akai-Kasaya , M.; Kuwahara , Y.; Mandal, S. K.; Aono, M. Controlled chain polymerisation and chemical soldering for single-molecule electronics. RSC: Nanoscale, 2012; Vol. 4, pp 3013-3028.

(25) Takajo, D.; Sudoh, K. Mechanism of Chain Polymerization in Self-Assembled Monolayers of Diacetylene on the Graphite Surface. *Langmuir* **2019**, *35* (6), 2123-2128. DOI: 10.1021/acs.langmuir.8b03737.

(26) van Meer, G.; Voelker, D. R.; Feigenson, G. W. Membrane lipids: where they are and how they behave. *Nature reviews. Molecular cell biology* **2008**, *9* (2), 112-124. DOI: 10.1038/nrm2330.

(27) Ilievski, F.; Mazzeo, A. D.; Shepherd, R. F.; Chen, X.; Whitesides, G. M. Soft Robotics for Chemists. *Angewandte Chemie (International ed.)* **2011**, *50* (8), 1890-1895. DOI: 10.1002/anie.201006464.

(28) Weibel, D. B.; Whitesides, G. M.; DiLuzio, W. R. Microfabrication meets microbiology. *Nature reviews. Microbiology* **2007**, *5* (3), 209-218. DOI: 10.1038/nrmicro1616.

(29) Wang, W. Y.; Pearson, A. T.; Kutys, M. L.; Choi, C. K.; Wozniak, M. A.; Baker, B. M.; Chen, C. S. Extracellular matrix alignment dictates the organization of focal adhesions and directs uniaxial cell migration. *APL bioengineering* **2018**, *2* (4), 046107-046107. DOI: 10.1063/1.5052239.

(30) Wagner, W. *Biomaterials science : an introduction to materials in medicine*; Academic Press, 2020.

(31) Chao, S.-h.; Carlson, R.; Meldrum, D. R. Rapid fabrication of microchannels using microscale plasma activated templating (microPLAT) generated water molds. *Lab on a chip* **2007**, *7* (5), 641-643. DOI: 10.1039/B618269K.

(32) Xia, Y. N.; Whitesides, G. M. Soft lithography. *Annual Review of Materials Science* **1998**, *28*, 153-184. DOI: 10.1146/annurev.matsci.28.1.153.

(33) Buluta, I.; Ashhab, S.; Nori, F. Natural and artificial atoms for quantum computation. *Reports on progress in physics* **2011**, *74* (10), 104401. DOI: 10.1088/0034-4885/74/10/104401.

(34) Lutolf, M. P.; Hubbell, J. A. Synthetic biomaterials as instructive extracellular microenvironments for morphogenesis in tissue engineering. *Nature Biotechnology* **2005**, *23* (1), 47-55.

(35) Zwaneveld, N. A. A.; Pawlak, R.; Abel, M.; Catalin, D.; Gimes, D.; Bertin, D.; Porte, L. Organized Formation of 2D Extended Covalent Organic Frameworks at Surfaces. *Journal of the American Chemical Society* **2008**, *130*, 6678-6679.

(36) Okawa, Y.; Aono, M. Linear chain polymerization initiated by a scanning tunneling microscope tip at designated positions. *The Journal of chemical physics* **2001**, *115* (5), 2317-2322. DOI: 10.1063/1.1384554.

(37) Groszek, A. J. Preferential Adsorption of Long-Chain Normal Paraffins on MoS_2, WS_2 and Graphite from n-Heptane. *Nature* **1964**, *204* (495), 680.

(38) Rabe, J. P.; Buchholz, S. Commensurability and Mobility in 2-Dimensional Molecular Patterns on Graphite. *Science* **1991**, *253* (5018), 424-427.

(39) Cyr, D. M.; Venkataraman, B.; Flynn, G. W. STM investigations of organic molecules physisorbed at the liquid-solid interface. *Chemistry of Materials* **1996**, *8* (8), 1600-1615.

(40) Giridharagopal, R.; Kelly, K. F. Substrate-Dependent Properties of Polydiacetylene Nanowires on Graphite and MoS2. *ACS Nano* **2008**, *2* (8), 1571-1580. DOI: 10.1021/nn800287x.

(41) Grim, P. C. M.; De Feyter, S.; Gesquiere, A.; Vanoppen, P.; Rucker, M.; Valiyaveettil, S.; Moessner, G.; Mullen, K.; De Schryver, F. C. Submolecularly resolved polymerization of diacetylene molecules on the graphite surface observed with scanning tunneling microscopy. *Angewandte Chemie-International Edition* **1997**, *36* (23), 2601-2603, Article. DOI: 10.1002/anie.199726011.

(42) Mandal, S. K.; Okawa, Y.; Hasegawa, T.; Aono, M. Rate-Determining Factors in the Chain Polymerization of Molecules Initiated by Local Single-Molecule Excitation. *ACS Nano* **2011**, *5* (4), 2779-2786. DOI: 10.1021/nn103231j.

(43) Okawa, Y.; Aono, M. Materials science Nanoscale control of chain polymerization. *Nature (London)* **2001**, *409* (6821), 683-684. DOI: 10.1038/35055625.

(44) Endo, O.; Ootsubo, H.; Toda, N.; Suhara, M.; Ozaki, H.; Mazaki, Y. Phase Transition of a Single Sheet of Sashlike Polydiacetylene Atomic Sash on a Solid Surface. *Journal of the American Chemical Society* **2004**, *126* (32), 9894-9895. DOI: 10.1021/ja047841g.

(45) Choong, S. W.; Russell, S. R.; Bang, J. J.; Patterson, J. K.; Claridge, S. A. Sitting Phase Monolayers of Polymerizable Phospholipids Create Dimensional, Molecular-Scale Wetting Control for Scalable Solution-Based Patterning of Layered Materials. *ACS applied materials & interfaces* **2017**, *9* (22), 19326-19334. DOI: 10.1021/acsami.7b03279.

(46) Davis, T. C.; Bechtold, J. O.; Hayes, T. R.; Villarreal, T. A.; Claridge, S. A. Hierarchically Patterned Striped Phases of Phospholipids: Toward Controlled Presentation of Carbohydrates. *Faraday Discussions* **2019**, *219*, 229-243.

(47) Hayes, T. R.; Lang, E. N.; Shi, A.; Claridge, S. A. Large-Scale Noncovalent Functionalization of 2D Materials through Thermally Controlled Rotary Langmuir-Schaefer Conversion. *Langmuir* **2020**, *36*, 10577-10586.

(48) Hoeppener, S.; Chi, L.; Fuchs, H. Formation of Au55 Strands on a Molecular Template at the Solid−Liquid Interface. *Nano letters* **2002**, *2* (5), 459-463. DOI: 10.1021/nl025522m.

(49) Mezour, M. A.; Perepichka, I. I.; Zhu, J.; Lennox, R. B.; Perepichka, D. F. Directing the Assembly of Gold Nanoparticles with Two-Dimensional Molecular Networks. *ACS nano* **2014**, *8* (3), 2214-2222. DOI: 10.1021/nn405357j.

(50) Bechtold, J. O.; Arango, J. C.; Shi, A.; Singh, A.; Claridge, S. A. Striped Poly(diacetylene) Monolayers Control Adsorption of Polyelectrolytes and Proteins on 2D Materials and Elastomers. *ACS applied nano materials* **2021**, *4* (7), 7037-7046. DOI: 10.1021/acsanm.1c01063.

(51) Tieke, B.; Wegner, G.; Naegele, D.; Ringsdorf, H. Polymerization of Tricosa-10,12-diynoic Acid in Multilayers. *Angewandte Chemie (International ed.)* **1976**, *15* (12), 764-765. DOI: 10.1002/anie.197607641.

(52) Okada, S.; Peng, S.; Spevak, W.; Charych, D. Color and Chromism of Polydiacetylene Vesicles. *Accounts of chemical research* **1998**, *31* (5), 229-239. DOI: 10.1021/ar970063v.

(53) Tieke, B.; Lieser, G.; Wegner, G. POLYMERIZATION OF DIACETYLENES IN MULTILAYERS. *Journal of Polymer Science Part a-Polymer Chemistry* **1979**, *17* (6), 1631-1644, Article. DOI: 10.1002/pol.1979.170170607.

(54) Olmsted, J.; Strand, M. Fluorescence of Polymerized Diacetylene Bilayer Films. *Journal of Physical Chemistry* **1983**, *87*, 4790-4792.

(55) Davis, T. C.; Russell, S. R.; Claridge, S. A. Edge-on adsorption of multi-chain functional alkanes stabilizes noncovalent monolayers on MoS_2. *Chemical Communications* **2018**, *54*, 11709-11712.

(56) Chance, R. R.; Patel, G. N. Solid-state polymerization of a diacetylene crystal: Thermal, ultraviolet, and γ-ray polymerization of 2,4-hexadiyne-1,6-diol bis-(p-toluene sulfonate). *Journal of polymer science. Polymer physics edition* **1978**, *16* (5), 859-881. DOI: 10.1002/pol.1978.180160511.

(57) Wegner, G. Topochemical reactions of monomers with conjugated triple bonds. III. Solid-state reactivity of derivatives of diphenyldiacetylene. *Journal of polymer science. Part B, Polymer letters* **1971**, *9* (2), 133-144. DOI: 10.1002/pol.1971.110090211.

(58) Yin, S.; Wang, C.; Qiu, X.; Xu, B.; Bai, C. Theoretical study of the effects of intermolecular interactions in self-assembled long-chain alkanes adsorbed on graphite surface. *Surface and interface analysis* **2001**, *32* (1), 248-252. DOI: 10.1002/sia.1047.

(59) Bain, C. D.; Whitesides, G. M. Molecular-Level Control over Surface Order in Self-Assembled Monolayer Films of Thiols on Gold. *Science* **1988**, *240* (4848), 62-63. DOI: 10.1126/science.240.4848.62.

(60) Lee, T. R.; Carey, R. I.; Biebuyck, H. A.; Whitesides, G. M. The Wetting of Monolayer Films Exposing Ionizable Acids and Bases. *Langmuir* **1994**, *10* (3), 741-749. DOI: 10.1021/la00015a024.

(61) Hibino, M.; Sumi, A.; Hatta, I. Molecular arrangements of fatty acids and cholesterol at liquid/graphite interface observed by scanning tunneling microscopy. *Japanese journal of applied physics* **1995**, *34* (6B), 3354-3359. DOI: 10.1143/JJAP.34.3354.

(62) de la Rosa, C. J. L.; Phillipson, R.; Teyssandier, J.; Adisoejoso, J.; Balaji, Y.; Huyghebaert, C.; Radu, I.; Heyns, M.; De Feyter, S.; De Gendt, S. Molecular doping of MoS2 transistors by self-assembled oleylamine networks. *Applied Physics Letters* **2016**, *109* (25). DOI: 10.1063/1.4972781.

(63) Whitesides, G. M. Soft Robotics. *Angewandte Chemie International Edition* **2018**, *57*, 4258-4273.

(64) Heikenfeld, J.; Jajack, A.; Rogers, J. A.; Gutruf, P.; Tian, L.; Pan, T.; Li, R.; Khine, M.; Kim, J.; Wang, J.; et al. Wearable sensors: modalities, challenges, and prospects. *Lab on a Chip* **2018**, *18*, 217-248.

(65) Davis, T. C.; Bang, J. J.; Brooks, J. T.; McMillan, D. G.; Claridge, S. A. Hierarchically Patterned Noncovalent Functionalization of 2D Materials by Controlled Langmuir–Schaefer Conversion. *Langmuir* **2018**, *34* (4), 1353-1362. DOI: 10.1021/acs.langmuir.7b03845.

(66) Shi, A.; Villarreal, T. A.; Singh, A.; Hayes, T. R.; Davis, T. C.; Brooks, J. T.; Claridge, S. A. Plenty of Room at the Top: A Multi-Scale Understanding of nm-Resolution Polymer Patterning on 2D Materials. *Angewandte Chemie (International ed.)* **2021**, *60* (48), 25436-25444. DOI: 10.1002/anie.202110517.

(67) Tieke, B.; Graf, H. J.; Wegner, G.; Naegele, B.; Ringsdorf, H.; Banerjie, A.; Day, D.; Lando, J. B. Polymerization of mono- and multilayer forming diacetylenes. *Colloid and polymer science* **1977**, *255* (6), 521-531. DOI: 10.1007/BF01549738.

(68) Rawiso, M.; Aime, J. P.; Fave, J. L.; Schott, M.; Muller, M. A.; Schmidt, M.; Baumgartl, H.; Wegner, G. Solutions of polydiacetylenes in good and poor solvents: a light and neutron scattering study. *Journal de Physique* **1988**, *49*, 861-880.

(69) Noel, S.; Liberelle, B.; Robitaille, L.; De Crescenzo, G. Quantification of Primary Amine Groups Available for Subsequent Biofunctionalization of Polymer Surfaces. *Bioconjugate chemistry* **2011**, *22* (8), 1690-1699. DOI: 10.1021/bc200259c.

(70) Cen, L.; Neoh, K. G.; Kang, E. T. Surface Functionalization of Electrically Conductive Polypyrrole Film with Hyaluronic Acid. *Langmuir* **2002**, *18* (22), 8633-8640. DOI: 10.1021/la025979b.

(71) Galanina, O. E.; Mecklenburg, M.; Nifantiev, N. E.; Pazynina, G. V.; Bovin, N. V. GlycoChip: multiarray for the study of carbohydrate-binding proteins. *Lab on a chip* **2003**, *3* (4), 260-265. DOI: 10.1039/b305963d.

(72) Bang, J. J.; Porter, A. G.; Davis, T. C.; Hayes, T. R.; Claridge, S. A. Spatially Controlled Noncovalent Functionalization of 2D Materials Based on Molecular Architecture. *Langmuir* **2018**, *34* (19), 5454-5463. DOI: 10.1021/acs.langmuir.8b00553.

(73) Hayes, T. R.; Lang, E. N.; Claridge, S. A. Large-Scale Noncovalent Functionalization of 2D Materials through Heated Roller Langmuir-Schaefer Conversion. *In preparation.* **2019**.

(74) Gur; Fromer, N. A.; Geier, M. L.; Alivisatos, A. P. Air-Stable All-Inorganic Nanocrystal Solar Cells Processed from Solution. *Science (American Association for the Advancement of Science)* **2005**, *310* (5747), 462-465. DOI: 10.1126/science.1117908.

(75) Carbone, L.; Nobile, C.; De Giorgi, M.; Sala, F. D.; Morello, G.; Pompa, P.; Hytch, M.; Snoeck, E.; Fiore, A.; Franchini, I. R.; et al. Synthesis and Micrometer-Scale Assembly of Colloidal CdSe/CdS Nanorods Prepared by a Seeded Growth Approach. *Nano letters* **2007**, *7* (10), 2942-2950. DOI: 10.1021/nl0717661.